



HAL
open science

The evolving interstellar medium of star-forming galaxies, as traced by Stardust

Vasily I. Kokorev, Georgios E. Magdis, Iary Davidzon, Gabriel Brammer, Francesco Valentino, Emanuele Daddi, Laure Ciesla, Daizhong Liu, Shuowen Jin, Isabella Cortzen, et al.

► To cite this version:

Vasily I. Kokorev, Georgios E. Magdis, Iary Davidzon, Gabriel Brammer, Francesco Valentino, et al.. The evolving interstellar medium of star-forming galaxies, as traced by Stardust. The Astrophysical Journal, 2021, 921 (1), pp.40. 10.3847/1538-4357/ac18ce . hal-03585129

HAL Id: hal-03585129

<https://amu.hal.science/hal-03585129v1>

Submitted on 12 Nov 2024

HAL is a multi-disciplinary open access archive for the deposit and dissemination of scientific research documents, whether they are published or not. The documents may come from teaching and research institutions in France or abroad, or from public or private research centers.

L'archive ouverte pluridisciplinaire **HAL**, est destinée au dépôt et à la diffusion de documents scientifiques de niveau recherche, publiés ou non, émanant des établissements d'enseignement et de recherche français ou étrangers, des laboratoires publics ou privés.

Copyright



The Evolving Interstellar Medium of Star-forming Galaxies, as Traced by Stardust*

Vasily I. Kokorev^{1,2}, Georgios E. Magdis^{1,2,3}, Iary Davidzon^{1,2}, Gabriel Brammer^{1,2}, Francesco Valentino^{1,2}, Emanuele Daddi⁴, Laure Ciesla^{4,5}, Daizhong Liu⁶, Shuowen Jin^{7,8}, Isabella Cortzen⁹, Ivan Delvecchio^{4,10}, Clara Giménez-Arteaga^{1,2}, Carlos Gómez-Guijarro⁴, Mark Sargent¹¹, Sune Toft^{1,2}, and John R. Weaver^{1,2}

¹ Cosmic Dawn Center (DAWN), Jagtvej 128, DK-2200 Copenhagen N, Denmark; vasilii.kokorev@nbi.ku.dk

² Niels Bohr Institute, University of Copenhagen, Blegdamsvej 17, DK-2100 Copenhagen Ø, Denmark

³ DTU-Space, Technical University of Denmark, Elektrovej 327, DK-2800 Kgs. Lyngby, Denmark

⁴ CEA, Irfu, DAp, AIM, Université Paris-Saclay, Université de Paris, CNRS, F-91191 Gif-sur-Yvette, France

⁵ Aix Marseille Univ, CNRS, CNES, LAM, Marseille, France

⁶ Max-Planck-Institut für Extraterrestrische Physik (MPE), Giessenbachstr. 1, D-85748 Garching, Germany

⁷ Instituto de Astrofísica de Canarias (IAC), E-38205 La Laguna, Tenerife, Spain

⁸ Universidad de La Laguna, Dpto. Astrofísica, E-38206 La Laguna, Tenerife, Spain

⁹ Institut de Radioastronomie Millimétrique (IRAM), 300 rue de la Piscine, F-38400 Saint-Martin-d'Hères, France

¹⁰ INAF—Osservatorio Astronomico di Brera, via Brera 28, I-20121, Milano, Italy & via Bianchi 46, I-23807, Merate, Italy

¹¹ Astronomy Centre, Department of Physics and Astronomy, University of Sussex, Brighton, BN1 9QH, UK

Received 2021 February 26; revised 2021 July 6; accepted 2021 July 10; published 2021 October 28

Abstract

We analyze the far-infrared (FIR) properties of ~ 5000 star-forming galaxies at $z < 4.5$, drawn from the deepest, super-deblended catalogs in the GOODS-N and COSMOS fields. We develop a novel panchromatic spectral energy distribution fitting algorithm, *Stardust*, that models the emission from stars, active galactic nuclei (AGNs), and infrared dust emission, without relying on energy balance assumptions. Our code provides robust estimates of the UV–optical and FIR physical parameters, such as the stellar mass (M_*), dust mass (M_{dust}), infrared luminosities (L_{IR}) arising from AGN and star formation activity, and the average intensity of the interstellar radiation field ($\langle U \rangle$). Through a set of simulations we quantify the completeness of our data in terms of M_{dust} , L_{IR} , and $\langle U \rangle$ and subsequently characterize the distribution and evolution of these parameters with redshift. We focus on the dust-to-stellar mass ratio (f_{dust}), which we parameterize as a function of cosmic age, stellar mass, and specific star formation rate. The f_{dust} is found to increase by a factor of 10 from $z = 0$ to $z = 2$ and appears to remain flat at higher z , mirroring the evolution of the gas fraction. We also find a growing fraction of warm to cold dust with increasing distance from the main sequence, indicative of more intense interstellar radiation fields, higher star formation efficiencies, and more compact star-forming regions for starburst galaxies. Finally, we construct the dust mass functions (DMFs) of star-forming galaxies up to $z = 1$ by transforming the stellar mass function to DMF through the scaling relations derived here. The evolution of f_{dust} and the recovered DMFs are in good agreement with the theoretical predictions of the Horizon-AGN and IllustrisTNG simulations.

Unified Astronomy Thesaurus concepts: High-redshift galaxies (734); Submillimeter astronomy (1647); Infrared astronomy (786); Astronomy software (1855); Galaxies (573); Active galaxies (17); Starburst galaxies (1570)

Supporting material: machine-readable table

1. Introduction

One of the main mechanisms driving galaxy evolution is the interaction between the interstellar medium (ISM), primarily consisting of gas and dust, and the radiation field induced by stellar activity. In this context, dust poses challenges in the detection of the UV/optical emission of galaxies and in the interpretation of these observations in terms of physical properties (e.g., star formation rate (SFR), stellar mass M_* , etc.), but it also is an important tracer of star formation and ISM in the far-IR (FIR) observations. At the same time, dust shields cold molecular hydrogen from ionizing photons and facilitates the collapse of molecular gas and subsequent star formation (Goldsmith 2001; Krumholz et al. 2011; Narayanan et al. 2011, 2012; Narayanan & Davé 2012). As such, dust plays a critical role in the life cycle of galaxies and offers observational signatures regarding their past evolutionary stages.

The impressive variety of infrared and millimeter facilities commissioned in the past few decades has propelled the

extragalactic ISM studies at an ever-increasing number, redshift, and detail. Indeed, the enormous observational efforts manifested by the large FIR/millimeter imaging and spectroscopic surveys such as PEP (Lutz et al. 2011), GOODS-Herschel (Elbaz et al. 2011), PHIBBS (Tacconi et al. 2013), S2CLS (Geach et al. 2017), and many others (e.g., Oliver et al. 2012; Magnelli et al. 2013; Walter et al. 2016; Dunlop et al. 2017; Saintonge et al. 2017; Maddox et al. 2018; Béthermin et al. 2020; Franco et al. 2020; Reiter et al. 2020; Valentino et al. 2020, for a review see Carilli & Walter 2013; Hodge & da Cunha 2020) have yielded a wealth of multiwavelength data sets and have advanced our understanding of galaxy evolution through scaling relations that have been used to guide simulations and theoretical models (e.g., Dekel et al. 2009; Popping et al. 2014; Lagos et al. 2015, 2020; Narayanan et al. 2015; Davé et al. 2017, 2020; Popping et al. 2017).

In the evolutionary picture that is emerging from the analysis of the FIR/millimeter surveys, the majority of star-forming galaxies (SFGs) follow a tight relation—the main sequence (MS)—between the SFR and M_* with an increasing normalization factor (specific SFR, $s\text{SFR} = \text{SFR}/M_*$) at least up to

* <https://github.com/VasilyKokorev/stardust/>

$z \sim 4$ (Brinchmann et al. 2004; Daddi et al. 2007; Elbaz et al. 2007, 2010, 2011; Noeske et al. 2007; Salim et al. 2007; Chen et al. 2009; Pannella et al. 2009; Santini et al. 2009; Daddi et al. 2010; Magdis et al. 2010; Oliver et al. 2010; Karim et al. 2011; Rodighiero et al. 2011; Shim et al. 2011; Lee et al. 2012; Reddy et al. 2012; Salmi et al. 2012; Whitaker et al. 2012; Zahid et al. 2012; Kashino et al. 2013; Moustakas et al. 2013; Rodighiero et al. 2014; Sargent et al. 2014; Sobral et al. 2014; Speagle et al. 2014; Steinhardt et al. 2014; Whitaker et al. 2014; Lee et al. 2015; Schreiber et al. 2015; Shivaei et al. 2015; Tasca et al. 2015; Whitaker et al. 2015; Erfanianfar et al. 2016; Kurczynski et al. 2016; Santini et al. 2017; Pearson et al. 2018; Leslie et al. 2020). This elevation of sSFR with look-back time, which broadly mirrors the overall increase of the SFR density of the universe from $z = 0$ to $z = 2 - 3$, is also followed by a similar rise in the gas fraction ($f_{\text{gas}} = M_{\text{gas}}/M_*$) of SFGs (e.g., Daddi et al. 2010; Geach et al. 2011; Magdis et al. 2012a, 2012b; Tacconi et al. 2013; Liu et al. 2019a, 2019b). Nevertheless, for fixed M_* , the increase in star formation efficiencies ($\text{SFE} = \text{SFR}/M_{\text{gas}}$) surpasses that in M_{gas} , resulting in higher SFR, an activity that, coupled with the observed M_* -size evolution (e.g., van der Wel et al. 2014), instills warmer luminosity-weighted dust temperatures of the ISM as a function of redshift (e.g., Magdis et al. 2012a, 2017; Magnelli et al. 2014; Béthermin et al. 2015; Casey et al. 2018; Schreiber et al. 2018; Liang et al. 2019; Cortzen et al. 2020).

Although the purity of the MS as a measure of the evolutionary stage of a galaxy has recently been challenged (e.g., Elbaz et al. 2018; Puglisi et al. 2019; Valentino et al. 2020), it appears that the majority of SFGs grow along the MS by secularly converting (and hence depleting) their gas mass reservoirs into stars (e.g., Daddi et al. 2010; Davé et al. 2012; Lilly et al. 2013; Tacchella et al. 2016), with a high degree of uniformity in the properties of their ISM (at fixed redshift). On the other hand, galaxies above the MS (starbursts (SBs)) are primarily characterized by elevated sSFR, SFE, and dust temperature (T_d) with respect to the average star-forming population at their corresponding redshift (e.g., Daddi et al. 2010; Magdis et al. 2012a; Magnelli et al. 2014; Scoville et al. 2017; Silverman et al. 2018; Tacconi et al. 2018). Galaxies below the MS are mainly post-SBs or quenched systems with low levels of star formation activity, low gas fractions, and cold T_d (e.g., Williams et al. 2021; Magdis et al. 2021).

At the core of the aforementioned results is the robustness of the derived FIR properties, namely, the total infrared luminosity (L_{IR}), the dust mass (M_{dust}), the mean intensity of the radiation field ($\langle U \rangle \propto L_{\text{IR}}/M_{\text{dust}}$), and T_d . These quantities and their emerging evolution with redshift rely on the availability of FIR/millimeter data and on selection effects. In this regard, while the ongoing ALMA observations are quickly filling the gap in resolution and sensitivity between the available UV/optical/near-IR (NIR) (subarcsecond) data and the coarse resolution of the confusion-limited SCUBA-2 and SPIRE/Herschel surveys, the vast majority of the SFG samples with available FIR photometry are still restricted to the latter. Thus, FIR studies are still largely focusing on the FIR luminous and most massive SFGs, on limited and possibly nonhomogeneous or biased ALMA samples, or on stacking techniques.

Moreover, the derived measurements of M_{dust} and T_d heavily rely on the adopted models and fitting techniques (e.g., Dale et al. 2014; Berta et al. 2016). Indeed, without a coherent and homogeneous treatment of the data sets it is impossible to

overcome systematic effects that could distort the observed trends. On top of that, recent high-resolution observations with ALMA indicate that the UV/optical and millimeter emissions of some high- z SFGs are spatially distinct (e.g., Hodge et al. 2016), posing challenges to the widely adopted energy balance assumption that is inherent in most multiwavelength fitting codes. Similarly, there is an ever-increasing number of IR-bright yet optically faint/dark sources (e.g., Wang et al. 2016; Casey et al. 2019; Jin et al. 2019; Franco et al. 2020) that an energy balance approach would have technical difficulties accommodating.

Finally, while many studies have focused on f_{gas} , the evolution of the dust fraction ($f_{\text{dust}} = M_{\text{dust}}/M_*$) and the dust mass function (DMF) with redshift has not been scrutinized to the same extent (Dunne et al. 2011; Magdis et al. 2012a; Santini et al. 2014; Tan et al. 2014; Béthermin et al. 2015; Driver et al. 2018; Donevski et al. 2020; Magnelli et al. 2020). Given that the use of M_{dust} as a proxy of M_{gas} either through the metallicity-dependent dust-to-gas mass ratio technique (e.g., Leroy et al. 2011; Magdis et al. 2011, 2012a; Eales et al. 2012; Berta et al. 2016; Tacconi et al. 2018) or (indirectly) through the monochromatic flux densities in the Rayleigh–Jeans (R-J) tail of the spectral energy distribution (SED; e.g., Groves et al. 2015; Scoville et al. 2017) has gained momentum, a proper investigation of the evolution of f_{dust} and DMF with redshift is necessary and remains to be done. More importantly, the f_{dust} , the DMFs, and in general the life cycle of dust are key in our understanding of metal enrichment processes and dust production mechanisms. These derived properties are also critical parameters of semianalytical and analytical models that couple the evolution of stars, metals, and gas (Lacey et al. 2016; Popping et al. 2017; Imara et al. 2018; Cousin et al. 2019; Lagos et al. 2019; Pantoni et al. 2019; Vijayan et al. 2019), as well as of cosmological simulations that also trace the dark matter component (Hayward et al. 2013; Narayanan et al. 2015; McKinnon et al. 2017; Aoyama et al. 2019; Davé et al. 2019).

These considerations provide motivation for a coherent and homogeneous analysis of the full population of IR galaxies that are detected in the recently constructed, state-of-the-art “super-deblended” FIR catalogs in two of the most extensively studied cosmological fields, the Great Observatories Origins Deep Survey North (GOODS-N; Dickinson et al. 2003) and the Cosmic Evolution Survey (COSMOS; Scoville et al. 2007). These catalogs are built using the “super-deblending” technique (Jin et al. 2018; Liu et al. 2018) that allows prior-based source extraction from highly confused Herschel and SCUBA +AzTEC maps, yielding robust UV to radio photometry for thousands of individually detected galaxies. To model the observed SEDs, we built and make publicly available a novel, time-efficient, and panchromatic SED fitting algorithm that we use to infer and explore the evolution and the variations of IR properties of SFGs (M_{dust} , T_d , $\langle U \rangle$, f_{dust} , f_{gas} , DMF) out to $z \sim 4$ and compare those to recent theoretical predictions. The catalogs with the derived FIR parameters for the full sample are also publicly released.

The paper is organized as follows. In Section 2 we describe the data sets used in this work, while Section 3 introduces our SED fitting algorithm. In Section 4 we perform various simulations to determine the robustness of our sample, as well as the limiting M_{dust} . Section 5 presents our physical estimates for each galaxy in the sample and their evolution with z . In Section 6 we analyze the evolution of f_{dust} and calculate the

DMF through the conversion of the stellar mass function (SMF). In Section 7 we constrain the evolution of f_{gas} and compare it to the literature results. We discuss the implications that our findings have in Section 8, and we present our main conclusions and summary in Section 9.

Throughout this paper we assume a flat Λ CDM cosmology with $\Omega_{\text{m},0} = 0.3$, $\Omega_{\Lambda,0} = 0.7$, and $H_0 = 70 \text{ km s}^{-1} \text{ Mpc}^{-1}$ and a Chabrier (2003) initial mass function (IMF).

2. Panchromatic Catalogs and Sample Selection

2.1. GOODS-N “Super-deblended” Catalog

We first consider the “super-deblended” photometric catalog (hereafter SDC1) constructed by Liu et al. (2018) using the FIR and submillimeter images in GOODS-N. These images come from the Herschel Space Observatory (PACS and SPIRE instruments; see Elbaz et al. 2011; Magnelli et al. 2013) and the ground-based facilities SCUBA-2 ($850 \mu\text{m}$; Geach et al. 2017) and AzTEC+MAMBO (1.16 mm ; Penner et al. 2011).

Several novelties introduced in SDC1 are particularly useful for our analysis. First, detections from deep Spitzer IRAC and Very Large Array 20 cm (Owen 2018) are used as a prior for the positions of the blended FIR/submillimeter sources. Second, the SED information from shorter-wavelength photometry is also used as a prior for subtracting lower-redshift sources. This substantially decreases blending degeneracies and allows for a robust photometry extraction of sources at longer wavelengths. Moreover, the authors estimated more realistic photometry uncertainties for each photometric measurement with extensive Monte Carlo simulations. These improvements allow for deeper detection limits and statistically reliable estimates (both measurements and uncertainties) in the FIR +millimeter bands.

The SDC1 contains 3306 priors in total, including over 1000 FIR+millimeter detections. All sources have photometric redshifts and stellar masses inferred by EAZY (Brammer et al. 2008) and FAST (Kriek et al. 2009) respectively, based on the 3D-HST UV-NIR (Skelton et al. 2014) and Pannella et al. 2015 GOODS-N catalogs. Following Liu et al. (2018), we extend the photometric coverage of the published SDC1 catalog to shorter wavelengths by cross-matching with the 3D-HST UV-NIR (Skelton et al. 2014) and Pannella et al. (2015) GOODS-N catalogs. Approximately half of the objects within the catalog are spectroscopically confirmed. However, as mentioned by the authors, the outer perimeter of the GOODS-N area contains objects with high instrumental noise in the $24 \mu\text{m}$ prior image that may impair the extraction process. We therefore choose to limit our analysis to the central 134 arcmin^2 with reliable photometry (flag $\text{goodArea}=1$ in SDC1). This reduced our final sample to 2344 objects.

2.2. COSMOS “Super-deblended” Catalog

We supplement our study with the “super-deblended” catalog (SDC2 hereafter) presented in Jin et al. (2018). The catalog covers 1.7 deg^2 in COSMOS, in the same bands as in SDC1, plus additional MAMBO data at 1.2 mm (Bertoldi et al. 2007).

In practice, the deblending methodology remains identical to that adopted in SDC1, with one primary difference: an additional step selecting a highly complete sample of priors in K_s band from the UltraVista catalogs (McCracken et al. 2012). The resulting $24 \mu\text{m}$ detections are then combined with the

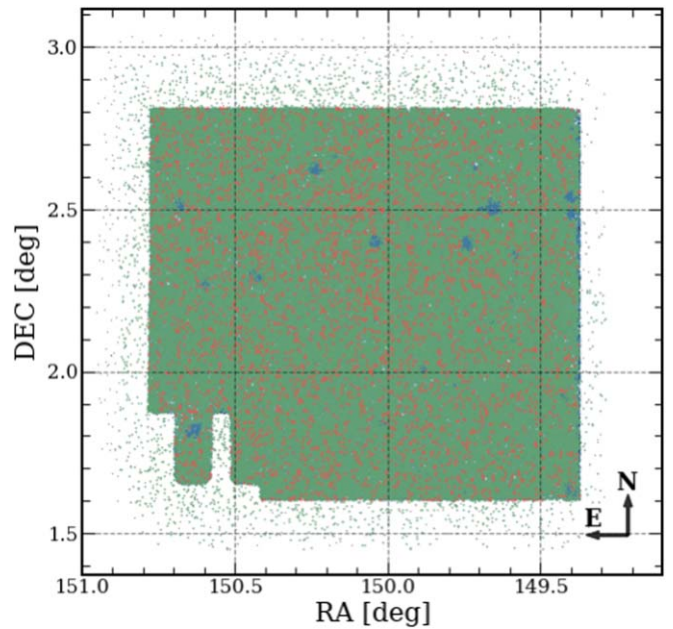


Figure 1. COSMOS sky map. The blue regions and black points represent sources from Muzzin et al. (2013) with $\text{goodArea} = 1$ and 0 , respectively (according to the quality flag in the Jin et al. 2018 catalog). The Laigle et al. (2016) coverage is shown in green. Sources that we use for our analysis are indicated in red.

mass-limited sample of K_s sources in order to fit the remaining bands in the catalog.

The final input data set contains 195,107 priors, with 13% of them having spectroscopic confirmation. The authors highlight that only 11,220 objects are in fact detected over the $100\text{--}1200 \mu\text{m}$ range. Similarly to GOODS-N, we impose the $\text{goodArea}=1$ flag to only include sources that are present in the UltraVista Data Release 4 area (McCracken et al. 2012). We note that for their catalog Jin et al. (2018) used a combination of Laigle et al. (2016) and Muzzin et al. (2013; hereafter M13) catalogs. The M13 catalog has an advantage in that it does not completely remove the sources around saturated stars, which has a positive effect on the number counts; however, the reduced quality of the photometry could lead to unreliable estimates for photometric redshifts (z_{phot}), as well as any parameters extracted by fitting optical templates. To be on the safe side, our analysis of SDC2 will only focus on the Laigle et al. (2016) sources, which narrows down the number of objects in the input catalog to 186,549 and the total area to 1.38 deg^2 . The COSMOS 2015 catalog (Laigle et al. 2016) also comes with a plethora of UV–optical photometry, spanning an additional ~ 20 bands, as well as photometric redshifts and stellar mass estimates by LePhare (Arnouts et al. 1999; Ilbert et al. 2006). We exploit these data by cross-matching the same COSMOS 2015 UV–optical photometry that was used to derive M_* and redshift to SDC2, thus extending our photometric coverage. In total, the merged catalogs consist of ~ 40 bands.

For posterity, in Figure 1 we present the UltraVista Data Release 2 map (Laigle et al. 2016; Davidzon et al. 2017) ($L16$ area), with the regions where the star subtraction took place being clearly identified. In addition to that, on the west border of the survey there exists a number of sources falling outside of the $L16$ area. These only have UltraVista coverage and lack additional Subaru photometry, which could affect the reliability of the z_{phot} .

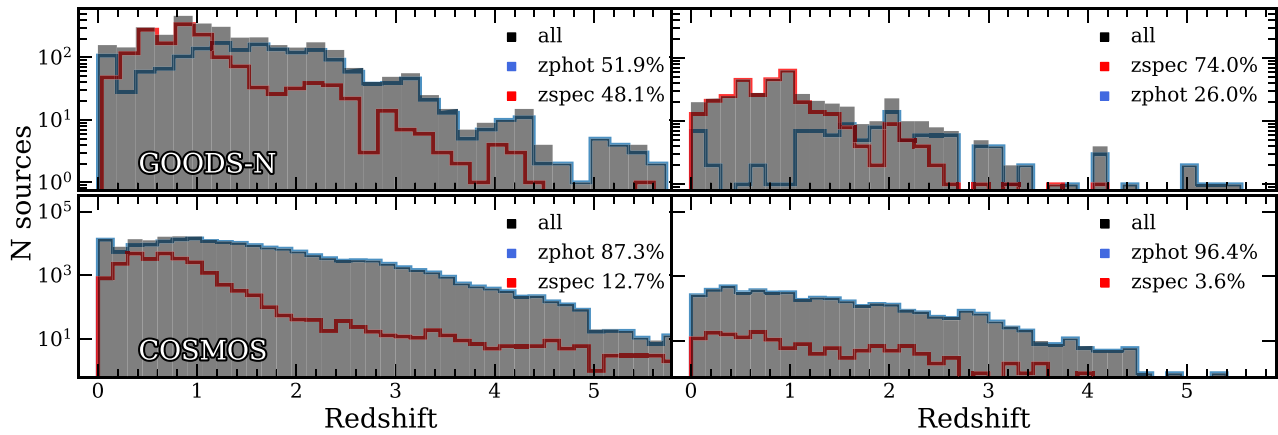


Figure 2. Redshift distributions of the sources considered in the present work. Both the photometric and spectroscopic redshifts were taken from the corresponding SDCs. The left and right panels show the redshift distribution of the original, full catalog and of the final sample that meets the selection criteria described in Section 2.3, respectively.

2.3. Sample Selection

The primary parameters that we can derive from observing the rest-frame FIR emission are the total infrared luminosity (L_{IR}), the dust mass (M_{dust}), and T_{d} or, equivalently, the intensity of interstellar radiation field ($\langle U \rangle$) in the Draine & Li (2007) dust model. To obtain robust estimates for these parameters, an adequate multiwavelength sampling of a galaxy’s SED is required. As such, constraining the IR peak is necessary for a robust L_{IR} estimate, while detections in the long-wavelength regime (R-J) are imperative to capture the emission from cold dust.

With these considerations in mind, after the initial cleaning of the catalogs described above, we perform our sample selection based on the following requirements:

1. Detection at a signal-to-noise ratio (S/N) > 3 significance in at least three FIR to submillimeter bands from $100 \mu\text{m}$ to 1.2 mm .¹²
2. Available z_{phot} (or z_{spec}) and M_{\star} estimates inferred by UV to NIR photometry.

After the quality cuts and the selection criteria, we are left with 4331 objects in COSMOS and 585 sources in GOODS-N, which constitute our sample. We have additionally identified 75 objects within SDC2 that fulfill our FIR detection criteria but, despite having a well-sampled UV–optical photometry, do not have either z_{phot} or M_{\star} estimates. We subsequently fit these sources with EAZY (Brammer et al. 2008), extract their z_{phot} and other UV–optical properties, and add them to our final catalog. This brings the total amount of COSMOS sources to 4406. The z_{phot} and z_{spec} distributions of the final sample in the two fields are presented in Figure 2 (right). As we will discuss later, a third criterion requesting at least one detection at $\lambda_{\text{rest}} > 150 \mu\text{m}$ will be imposed in order to define a subsample with robust M_{dust} estimates.

3. SED Fitting

3.1. The Inventory of Available SED Fitting Routines

Prior to providing the description of our methodology, we believe that it is important to outline and present a brief introduction of the available SED fitting codes that deal with a

three-component fitting approach, namely, combining the optical, active galactic nucleus (AGN), and dust emissions. These include the well-established and widely used energy balance routines such as CIGALE (Burgarella et al. 2005; Noll et al. 2009; Boquien et al. 2019), MAGPHYS (da Cunha et al. 2008; Battisti et al. 2019), and its AGN template extension presented in Chang et al. (2017). These have inspired more novel and sophisticated approaches that optimize the template libraries to achieve significant improvements in computational speeds (SED3FIT; Berta et al. 2013), or adopt Markov Chain Monte Carlo methods when extracting best-fit parameters such as AGNfitter (Calistro Rivera et al. 2016) and Prospector- α (Leja et al. 2018). These efforts are not just limited to published software packages, with many authors implementing their own routines for a panchromatic model analysis (see, e.g., Feltre et al. 2013; Symeonidis et al. 2013).

3.2. Basic Description of the Stardust Fitting Code

To model the extensive photometric coverage of the galaxies in our sample, we develop a new, panchromatic SED fitting tool: Stardust. The code performs a multicomponent fit that linearly combines stellar libraries with AGN torus templates and IR models of dust emission arising from star formation (SF-IR). This approach, which is very similar to that presented in Liu et al. (2021), has a number of key differences compared to the currently existing SED fitting codes such as MAGPHYS, CIGALE, and SED3FIT.

First, the three components (stellar, AGN, and SF-IR) are fit simultaneously yet independently from each other, without assuming an energy balance between the absorbed UV/optical radiation and the IR emission. The energy balance approach relies on the assumption that fitted stellar and dust emissions are copatial, i.e., the process of UV absorption and subsequent reemission at IR wavelength happen in the same environment (da Cunha et al. 2008; see, e.g., their Sections 2.1 and 2.2). However, the detected stellar and dust distributions within a galaxy are not always physically connected. Resolved observations of high- z dusty SFGs (DSFGs; Simpson et al. 2015; Hodge et al. 2016; Franco et al. 2018; Gómez-Guijarro et al. 2018; Hodge et al. 2019; Kaasinen et al. 2020) have revealed spatial offsets between the extent of the dust and stellar emitting sizes of high- z DSFGs, with the former being on average more compact (e.g., Chen et al. 2017; Tadaki et al. 2017; Calistro Rivera et al. 2018;

¹² Three bands are also required to reduce fitting degeneracies.

Cochrane et al. 2021). While energy balance is anticipated to apply universally, the aperture and sensitivity limitations of our observations cast a concern on how reliably we can bring these components together in the same panchromatic fit. These observations are also theoretically supported by radiative transfer codes (e.g., SKIRT; Cochrane et al. 2019) and hydrodynamical simulations (e.g., IllustrisTNG; Pillepich et al. 2019; Popping et al. 2021).

Moreover, the detection of “HST-dark” galaxies, i.e., sources that are undetected in the UV/optical bands and thus do not have the photometry to constrain either dust absorption or stellar emission but are bright in the IRAC and FIR/millimeter bands (Wang et al. 2016; Franco et al. 2018), poses another technical challenge to the correct application of the energy balance approach. Finally, the manner in which dust and stellar emission are connected, by assuming a single dust attenuation law and dust composition, can have a significant impact on derived parameters, as these recipes have been shown not to apply universally (Buat et al. 2019). In summary, while the premise of the energy balance routines is undoubtedly elegant and in most cases physically motivated, we choose to use independent stellar, AGN, and dust components to better focus on the dust properties themselves.

Furthering this complex picture, it is important to note the presence of cold diffuse dust, which is being heated by an older stellar population, rather than an ongoing star formation activity (see Boquien et al. 2011; Bendo et al. 2012; Galametz et al. 2014; Hayward et al. 2014). However, when dealing with nonresolved observations, the diffuse dust and R-J tail emissions are highly degenerate, and as such none of the aforementioned codes, nor *Stardust*, utilize these templates.

The other advantage of *Stardust* is related to the χ^2 minimization approach to select the best-fit models. Instead of finding the solution from a vast library of precompiled templates, we devise an optimization method to find the best linear combination of a much smaller set of “basic” templates (similar to eigenvectors in principal component analysis). This is the same approach adopted in the photometric redshift fitting code EAZY (Brammer et al. 2008). In our case, the basic templates are divided into three classes and the linear combination includes a sum of templates from these classes. The models used to create these templates are the following:

1. Stellar library. We incorporate an updated version of the stellar population synthesis (SPS) models described in Brammer et al. (2008). Although UV and optical photometry is not always available, the inclusion of the stellar component in the code is important in the NIR regime. In particular, it allows us to better constrain the AGN contribution (see Figure 18 and Appendix A). This stellar library represents an optimized basis set, where the nonnegative linear combinations of models can be considered to be the “principal components” of a much larger parent template catalog (see Brammer et al. 2008; Blanton & Roweis 2007).
2. AGN library. We adopt empirically derived templates from Mullaney et al. (2011) describing AGN intrinsic emission from 6 to 100 μm .¹³ We include both high- and low-luminosity templates (total of 2). Since these can be

linearly combined, we do not include the median luminosity AGN template.

3. Infrared library. It consists of 4862 Draine & Li (2007, hereafter DL07) templates, with the additional updates from Draine et al. (2014; see also Aniano et al. 2020). These models describe the contribution from warm dust and polycyclic aromatic hydrocarbon (PAH) features in the photodissociation regions (PDRs), together with cold dust in the diffuse part of the ISM. We consider¹⁴ a wide array of values for the minimum radiation field (U_{min}) in the $0.1 < U_{\text{min}} < 50$ range, as well as the fraction of the total dust mass locked in PAHs (q_{PAH}) between 0% and 10%. We have fixed $U_{\text{max}} = 10^6$ and $\alpha = 2$, as described in Magdis et al. (2012a). These templates are not linearly combined within their class; the algorithm instead chooses a single best-fit DL07 template.
4. Radio continuum. Data points in radio are not considered by our fitting routine; however, they can be used a posteriori to quantify possible radio excess and further confirm the presence of an AGN, if needed. Our radio model is based on the radio–FIR correlation, described in Delvecchio et al. (2021), with a spectral index of -0.75 .

More details on the characteristics of the templates and the motivation for selecting them are provided in Appendix A. With such a configuration, fitting a single object (including the computation of the uncertainties) with *Stardust* takes less than 10 s,¹⁵ i.e., a factor of 8–10 faster than software like CIGALE (see Appendix C), based on large precompiled template sets. If we choose to precompile all of our templates, instead of linearly combining them, the resulting model library would contain millions of possible SEDs, with computation time increasing by a significant amount. The code is also highly parallelized, which allows it to run on multiple threads simultaneously, thus achieving significant computation speeds on modern CPUs.

3.3. Configuration of the Code

For each object, the input consists of measured flux densities, their corresponding uncertainties, and a redshift estimate.¹⁶ The user must then choose the corresponding filter curves from the precompiled set, or upload their own. The individual template components can be switched off and on as an additional user input. The algorithm then outputs the best-fit FIR, as well as AGN properties of the source. If the photometry is available, the UV–optical parameters are also produced. These can be summarized as follows:

1. The total infrared luminosity integrated over the SF-IR +AGN templates ($L_{\text{IR,total}}$),¹⁷ the total infrared luminosity associated with star formation ($L_{\text{IR,DL07}}$), and the relative contribution of the PDR component (f_{PDR}) to $L_{\text{IR,DL07}}$.
2. The bolometric IR luminosity of the AGN (L_{AGN}) and its fractional contribution (f_{AGN}) to the total IR energy budget.¹⁸

¹⁴ The modular structure of the code allows the user to decide which DL07 templates to use.

¹⁵ Tested on a i9-8950HK CPU.

¹⁶ It is also possible to manually define a rectangular filter at a desired wavelength, for cases where the filter transmission curve is not easily obtainable, e.g., ALMA.

¹⁷ In this work we use terms L_{IR} and $L_{\text{IR,total}}$ interchangeably.

¹⁸ The quality of the photometry in this work does not allow us to distinguish bolometric AGN contributions below $\sim 0.5\%$, and thus the nonzero entries below that threshold are treated here as zero.

¹³ Note: these templates do not account for X-ray-selected QSOs. The flexible nature of the code, however, allows these templates to be manually injected if necessary.

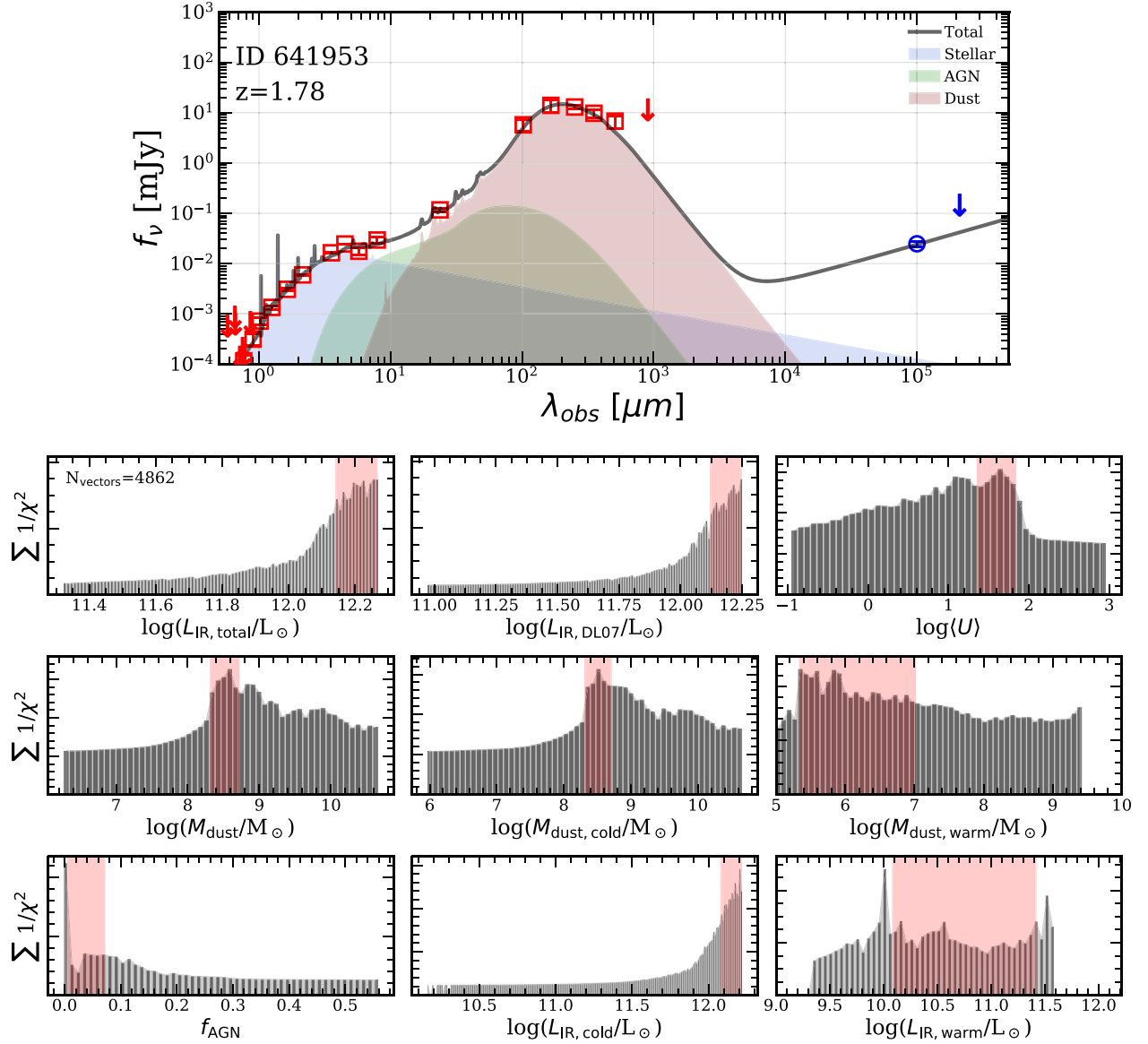


Figure 3. Top: example of an observed and best-fit SED, as obtained with the `Stardust` code for a $z_{\text{phot}} = 1.78$ galaxy (ID641953) drawn from the SDC2 sample. The squares and circles represent the $S/N > 3$ photometric detections, while 3σ upper limits are shown as downward-pointing arrows. Red symbols represent the SDC2 photometry that was used in our fitting routine, while blue symbols show the radio measurements at 1.4 and 3 GHz that were not included in the fit. Instead, the radio part of the model SED is based on the $L_{\text{IR}}-L_{1.4\text{ GHz}}$ relation of Delvecchio et al. (2021). The shaded red, green, and blue regions correspond to the dust, AGN, and stellar components, respectively. A linear combination of all three is given by a solid black line. Bottom: the χ^2 distributions for the main derived parameters. The shaded red areas enclose solutions for which $\Delta\chi^2 = 1$.

3. The total dust mass (M_{dust}), the warm dust mass component heated by PDRs ($M_{\text{dust}}^{\text{warm}}$), the fraction of the total dust mass heated by PDRs (γ), the cold dust mass component ($M_{\text{dust}}^{\text{cold}}$) in the diffuse ISM, and the fraction of the total dust mass locked in PAHs q_{PAH} .
4. The intensity of the radiation field that the diffuse ISM is exposed to (U_{min}), which is a proxy of the mass-weighted T_{d} of the ISM, and the mean radiation field intensity ($\langle U \rangle$), which is a proxy of the luminosity-weighted T_{d} .
5. The stellar mass (M_{\star}), star formation history (SFH), $E(B - V)$, and the unobscured SFR, if there is available optical photometry.

Figure 3 presents an example fit to one of the COSMOS galaxies, chosen for its prominent AGN contribution. The top

panel of the figure shows the data points and the best-fit model, with different colors for the four components listed above; the bottom panel displays the χ^2 distributions of all relevant IR quantities.

3.4. Derivation of Uncertainties

In order to estimate the errors associated with the derived quantities during the fitting procedure of `Stardust`, we consider two main sources of uncertainty: one concerning the linear combination coefficients of the best-fit optimization, and one linked to the broadband photometric data.

To quantify the linear combination uncertainty, we resample the best solution coefficients. A covariance matrix is first created by considering all of the templates that went into the

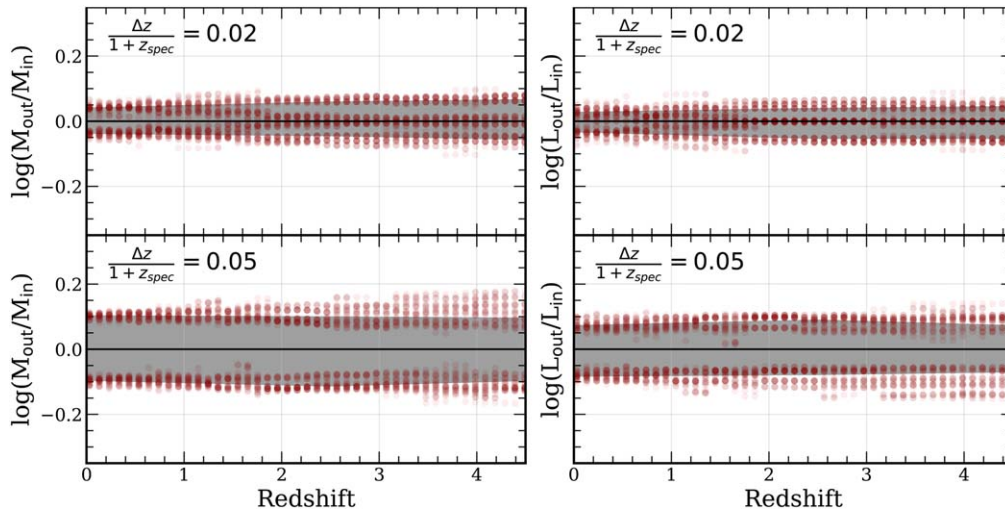


Figure 4. Effect of the z_{phot} uncertainty in the derivation of M_{dust} (left panel) and L_{IR} (right panel) assuming $\epsilon = 0.02$ (top) and $\epsilon = 0.05$ (bottom). Red circles represent the ratio of the output to input quantities from our simulations, as inferred by shifting the fitted redshift by $\pm \Delta z$. The shaded regions cover the 68% confidence interval, and the solid black line indicates a ratio equal to unity.

best-fit solution. We draw the coefficients from a multivariate normal distribution whose median is given by the coefficient of the best solution vector and the standard deviation is computed from the diagonalized covariance matrix. This is done 10^4 times to provide a good balance between robustness of the error estimates and computational speed. We recompute all the relevant FIR properties for each realization of our routine. From resultant distributions we then define our lower and upper uncertainty as the 16th and 84th percentile confidence interval, respectively. However, given the fact that only a single solution with a single coefficient is considered in the IR, the final uncertainty on the FIR properties is underestimated.

We therefore also consider the observational uncertainty, which is primarily driven by the quality of the photometric data. We compute it by considering all possible solutions from our template library that fall within the 68% confidence interval range of the best-fit. This would correspond to a region where the solutions fall within $\Delta\chi^2_\nu = 1$, where $\Delta\chi^2_\nu = \chi^2_{\nu,i} - \chi^2_{\nu,\text{best}}$, since the nondiagonal terms of the template covariance matrix are not zero.¹⁹ We show these as red shaded areas on the bottom panel of Figure 3. The observational uncertainty is then derived as simply the width of the shaded region.

The final errors are computed as a quadrature sum of the linear combination uncertainty and the observational uncertainty.

3.5. The Effect of Photometric Redshift Uncertainty

To explore and quantify how the uncertainty in z_{phot} propagates into the estimates of L_{IR} and M_{dust} , we built mock IR SEDs of 1200 galaxies utilizing a suite of $0.1 < U_{\text{min}} < 50$ DL07 models and place them uniformly in the $0.03 < z_{\text{true}} < 5$ redshift range. Thus, each mock SED is characterized by a set of predefined $L_{\text{IR,in}}$, $M_{\text{dust,in}}$, and z_{true} values. We then infer synthetic broadband photometry in all IR bands available in SDC2 (24–1100 μm) for each simulated galaxy. Since we are interested in the effect of the z_{phot} uncertainty on the derived FIR properties, to minimize any other possible sources of error (e.g., photometric uncertainty, poor photometric sampling of the SED), we adopt $S/N = 5$ in all bands and add to our photometric data set the monochromatic flux

density of the template at 2.2 mm. We then fit the synthetic photometry of each galaxy by fixing the redshift first to $z_- = z_{\text{true}} - \Delta z$ and then to $z_+ = z_{\text{true}} + \Delta z$, where $\Delta z = \epsilon(1 + z_{\text{true}})$. For our purposes, and based on the z_{phot} accuracy of the COSMOS field ($\epsilon = 0.005\text{--}0.03$ as quantified in L16), we first adopt $\epsilon = 0.02$ and then repeat the analysis for an even more conservative case with $\epsilon = 0.05$. The comparison between the extracted $L_{\text{IR,out}}$ and $M_{\text{dust,out}}$ to the input values for each simulation is presented in Figure 4.

Our analysis suggests that the effect Δz has in the derivation of the FIR properties is not negligible, even for the idealized case of detailed (24 μm –2.2 mm) and high-quality ($S/N = 5$) photometric coverage. Indeed, we find that a typical value of $\epsilon = 0.02$ ($\epsilon = 0.05$) introduces an extra scatter of $\sim 12\%$ (25%) and $\sim 17\%$ (35%) in the derived L_{IR} and M_{dust} , which remains rather constant with redshift (at least out to $z = 4$). At the same time, we also find that a symmetric Δz , such as the one adopted in our simulations, does not inflict a noticeable systematic offset in the extracted FIR quantities (< 0.05 dex).

Based on these results, we update the uncertainties of the inferred FIR properties of our z_{phot} sample ($z_{\text{type}} = 0$; see Appendix A) by adding in quadrature the extra error arising from a symmetric Δz (assuming $\epsilon = 0.02$ for all sources) to the error budget inferred by the SED fitting procedure (photometry + model). While our correction is based on an average value of $\epsilon = 0.02$, we note that for catastrophic z_{phot} failures ($\epsilon \sim 0.15$) we find a systematic offset of $\leq 30\%$ between the input versus output M_{dust} , while the L_{IR} ratios remain uniformly scattered around unity.

4. Completeness and Systematics

By construction, the photometric catalogs considered in this work combine observations that span ~ 4 orders of magnitude in wavelength range, have different sensitivity limits, and are differently affected by source blending and confusion. The fact that we choose to draw our sample based on the criteria described in Section 2, rather than selecting galaxies detected in a single band (i.e., a flux-limited sample), necessitates a series of simulations in order to quantify possible biases, systematic

¹⁹ See Sections 15.1 and 15.6 of Press et al. (1986) and Avni (1976). Note that $\Delta\chi^2_\nu = 1$ only applies when marginalized over all other parameters.

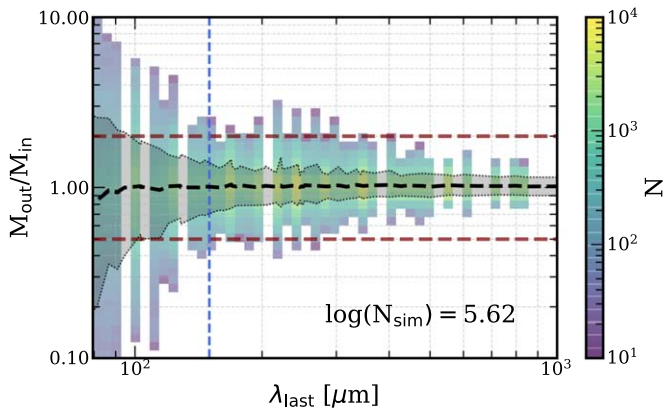


Figure 5. Accuracy of the inferred M_{dust} estimates as a function of (rest-frame) λ_{last} , parameterized by the ratio of the output to input M_{dust} in our simulations. The color-coding illustrates the density of the data points. The dashed black line and the shaded gray area denote the median and the 16th and 84th percentile confidence intervals, respectively. The dashed maroon lines represent the value where the M_{dust} ratio is 0.5 and 2. The vertical blue line at $150 \mu\text{m}$ denotes the λ_{last} onward where for $\geq 68\%$ of the simulated galaxies the accuracy of the recovered M_{dust} is $\geq 70\%$. The quantization along the x -axis is a consequence of the step size in redshift, along with the available observed bands.

effects, and the completeness of our sample in terms of M_{dust} and L_{IR} .

4.1. The Effect of λ_{last} Cutoff

It has been well established that for a robust modeling of the M_{dust} at least one photometric data point longward of the FIR peak, i.e., into the R-J tail of the SED, is necessary (e.g., Draine et al. 2007; Magdis et al. 2012a; Berta et al. 2016; Scoville et al. 2017). Here we attempt to quantify how the accuracy of the derived M_{dust} estimates varies as a function of the rest-frame wavelength of the last available detection in conjunction with the selection criteria of our sample (i.e., at least three detections at $24 \mu\text{m} < \lambda \leq 1200 \mu\text{m}$). For this, we perform the following simulations.

We start by building mock IR SEDs of fixed M_{dust} and L_{IR} , with $0.1 < U_{\text{min}} \leq 50$, $0 \leq \gamma \leq 0.5$, and $q_{\text{PAH}} = 2.8\%$, using the DL07 library and place them at $0.01 \leq z \leq 4.5$ with a step of $\Delta z = 0.05$. After all of the models are created, synthetic photometry is performed by convolving each mock redshifted SED with a filter transmission curve. We consider all filters redder than MIPS $24 \mu\text{m}$ available in SDC2, for a total of nine bands, and set all recovered fluxes to an $S/N = 3$ significance level. At each redshift the algorithm calculates the rest-frame wavelength for each available band, producing a grid of possible rest-frame wavelengths of the last detection (λ_{last}) after accounting for our selection criterion that requests the availability (and the detection) in at least two bluer bands. For each λ_{last} it then randomly selects two additional bands blueward of λ_{last} , producing a final set of three photometric data points. We then fit each set, as well as 50 permutations by varying the original fluxes by 10%, with our code to extract M_{dust} and L_{IR} estimates. This procedure is then repeated for all mock SEDs and all acceptable values of λ_{last} in each redshift.

The accuracy with which we can recover M_{dust} estimates for each λ_{last} is then quantified by the scatter of the ratio of output to input M_{dust} presented in Figure 5. As expected, we find a decreasing scatter in $M_{\text{dust,out}}/M_{\text{dust,in}}$ at longer λ_{last} , which

drops from a factor of ~ 2 (for 68% of the simulated galaxies) at $\lambda_{\text{last}} = 100 \mu\text{m}$ to a factor of ~ 1.1 at $\lambda_{\text{last}} = 400 \mu\text{m}$.

Based on these results, we choose to define the subsample of “ $M_{\text{dust-robust}}$ ” galaxies, for which at least one detection at $\lambda_{\text{last}} \geq 150 \mu\text{m}$ is available. This threshold was chosen as an optimal compromise between the number of the rejected sources and the precision of the derived M_{dust} , which for $\lambda_{\text{last}} \geq 150 \mu\text{m}$ is $\geq 70\%$. Indeed, while $\lambda_{\text{last}} \geq 150 \mu\text{m}$ is evidently not deep into the R-J, it seems that the addition of the two extra data points blueward of $\lambda_{\text{rest}} = 150 \mu\text{m}$ is adequate to anchor the general shape, and eventually the M_{dust} , of the templates.

As a sanity check for the effectiveness of our criterion, we cross-match the “ $M_{\text{dust-robust}}$ ” sample with the A3COSMOS ALMA photometric catalog presented in Liu et al. (2019a) and refit the 233 galaxies that we find in common, adding this time the extra ALMA data point to the input photometry. The comparison of the inferred $M_{\text{dust,A3}}$ to our M_{dust} estimates yields a very good agreement between the two estimates with a median $\log(M_{\text{dust,A3}}/M_{\text{dust}}) \approx -0.04 \pm 0.06$, further supporting our analysis. Nevertheless, we do identify a handful of sources for which the addition of the ALMA data point results in lower M_{dust} estimates by a factor of ≥ 3 . An inspection of the SEDs of these extreme outliers reveals that the discrepancy originates either from possible catastrophic blending of the SPIRE $500 \mu\text{m}$ photometry or alternatively from overresolved ALMA photometry.²⁰

The emerging “ $M_{\text{dust-robust}}$ ” sample consists of 3312 sources drawn from the same M_* and redshift distributions as the 4991 originally selected galaxies. Finally, we note that our simulations operate under the assumption that the DL07 models are a good representation for the FIR emission of the real galaxies. Variations in dust composition, dust emissivity, and dust absorption coefficients that could result in systematic offsets in the inferred M_{dust} (e.g., Dale et al. 2012; Magdis et al. 2012a; Berta et al. 2016; Scoville et al. 2017) cannot be modeled with our approach. As is the case for any other M_{dust} analysis, the relative rather than the face-value estimates bare more physical significance.

4.2. Limiting M_{dust} and L_{IR}

We now attempt to compute the completeness threshold of our sample in terms of M_{dust} and L_{IR} as a function of redshift. Again, we build a grid of mock IR SED in the $z = 0-5$ range using the same approach as described above. However, instead of considering the full range of possible $\langle U \rangle \propto L_{\text{IR}}/M_{\text{dust}}$ values of the DL07 models, the constructed templates this time follow the $\langle U \rangle$ - z relation of MS galaxies presented in Béthermin et al. (2015). At each redshift we then create a grid of templates normalized to $\log(M_{\text{dust}}/M_{\odot}) = 6-10$ in steps of 0.1.

As before, the templates are used to produce synthetic photometry for each template in all bands available in the SDC2 catalog. For each band we then adopt an rms based on the depth of the corresponding survey at each wavelength in the COSMOS field (Jin et al. 2018) and impose the same selection criteria on the mock photometry as those applied to the real catalogs. Following Section 4.1, we also request that the simulated sources have $\lambda_{\text{last}} \geq 150 \mu\text{m}$. If a galaxy of given M_{dust} fulfills these criteria at a given redshift, the algorithm

²⁰ The SEDs of the most extreme outliers can be retrieved at https://github.com/VasilyKokorev/sdc_ir_properties/.

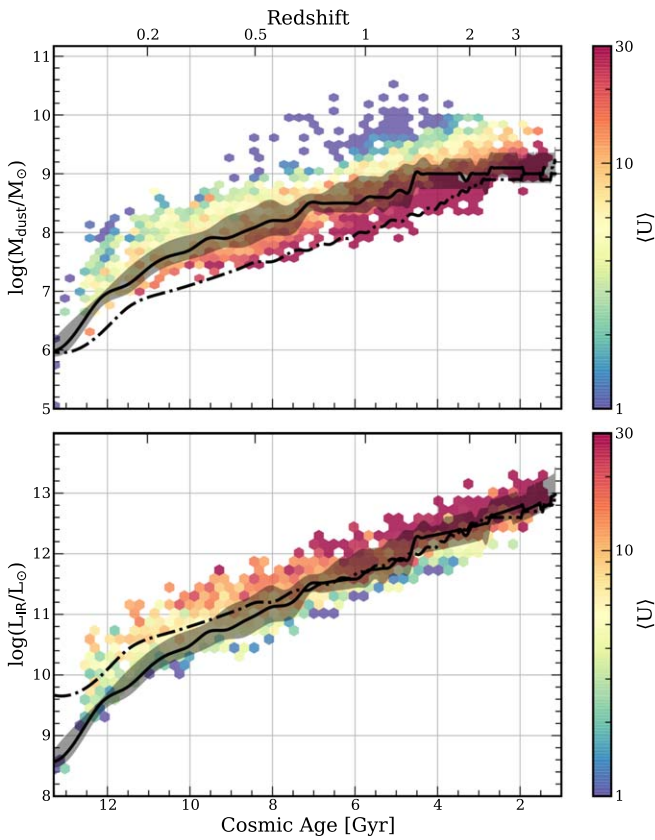


Figure 6. Simulated evolution of the $\text{lim}(M_{\text{dust}}(z))$ (top) and $\text{lim}(L_{\text{IR}}(z))$ (bottom), as described in Section 4.2. The black line represents the derived trend for MS galaxies, and the dashed–dotted line shows the same relations for SBs ($\langle U \rangle \sim 40$). The shaded regions define the 16th and 84th percentile confidence intervals, based on the scatter of the $\langle U \rangle$ – z relation from Béthermin et al. (2015). The hexagonal bins contain the inferred parameters of the “ M_{dust} –robust” sample (i.e., at least one detection at $\lambda \geq 150 \mu\text{m}$), color-coded by mean radiation field intensity $\langle U \rangle$.

moves to a lower M_{dust} until the object is rejected by our selection. By following these steps at different redshifts, we thus obtain a limiting M_{dust} as a function of z , which we coin $\text{lim}(M_{\text{dust}}(z))$. In the process we also consider the scatter of the $\langle U \rangle$ – z relation of Béthermin et al. (2015), in order to account for the variation of $\langle U \rangle$ among MS galaxies at a given redshift. The derived $\text{lim}(M_{\text{dust}}(z))$ can then be converted to $\text{lim}(L_{\text{IR}}(z))$, via

$$\langle U \rangle = \frac{L_{\text{IR,DL07}}}{125 M_{\text{dust}}}, \quad (1)$$

as described in Draine & Li (2007).

We also repeat our simulation for SBs, by fixing $\langle U \rangle = 40$ (e.g., Magdis et al. 2012a; Tan et al. 2014; Béthermin et al. 2015). We note, however, that the $\langle U \rangle$ of SBs can vary substantially to lower or higher values (e.g., Magdis et al. 2012a, 2017; Schreiber et al. 2018; Jin et al. 2019; Cortzen et al. 2020). Therefore, the chosen $\langle U \rangle = 40$ is only representative, but not necessarily unique. Nevertheless, $\langle U \rangle < 40$ templates are represented in the simulation of the MS galaxies, while galaxies with $\langle U \rangle > 40$ are rather rare.

The results of our simulations are presented in Figure 6, where we show the derived M_{dust} and L_{IR} as a function of z for the whole sample, along with the evolution of $\text{lim}(M_{\text{dust}})$ and $\text{lim}(L_{\text{IR}})$. We see that the limiting M_{dust} increases toward high z , peaking at $z \sim 2$, and remains flat afterward, signifying that the balance between cosmological dimming and negative K -correction is

achieved beyond that point. Following the black line, we could infer the M_{dust} threshold above which our sample should be 100% complete, assuming an MS-like population of galaxies. However, since our sample is not limited to MS galaxies, we naturally also find sources that fall below our limiting M_{dust} track. As we will discuss later, these are predominately starbursting galaxies that exhibit elevated $\langle U \rangle$ with respect to the MS. Our secondary $\text{lim}(M_{\text{dust}})$ trend for an SB-like population displays that with the SDC2 detection limits it is possible to detect a low- M_{dust} object only if it is also an SB.

We also find a similar trend for MS galaxies when considering the evolution of $\text{lim}(L_{\text{IR}})$. In this case, however, we do not observe a flattening at $z \sim 2$, and the trend continues to rise into the early universe. The balance between cosmological dimming and the negative K -correction is not being achieved here, since the wavelengths that are required to reliably constrain the L_{IR} are positioned to the left of the FIR peak.

Admittedly, depths of FIR surveys are not the only limiting factors of sample selection. A requirement to have a photometric redshift and M_* would mean that the optical photometry has to be sufficiently sampled, to allow such an analysis. Moreover, the deblending procedure itself goes through various selection stages, including both brightness and mass cuts. Various IR studies (Wang et al. 2016; Franco et al. 2018) have revealed substantial populations of optically dark sources at $2 < z < 4$, which are otherwise bright in IRAC and FIR bands, which would be unintentionally excluded from our analysis. Moreover, even at low z , objects that are faint in the K band would also be missed. Indeed, a combination of these factors creates significant obstacles in our completeness analysis; we address this in more detail in Section 6.2.

5. Far-infrared Properties of GOODS-N and COSMOS Galaxies

Using our newly developed code presented in Section 3, we extract the FIR and UV–optical properties for all 4991 galaxies from the SDC1 and SDC2 that meet our selection criteria as listed in Section 2. Moreover, since both input catalogs contain M_* estimates provided by LePhare, EAZY, or FAST, we are able to carry out a comparison of these M_* to the ones derived by Stardust. We find that the stellar masses are consistent with one another and direct the reader to Appendix B for a more detailed comparison between the two methods, as well as to EAZY-derived M_* . Despite the similarities between the available and derived M_* , in our subsequent analysis, we will utilize the M_* from the parent catalog, unless it is specified otherwise. This is done to preserve the original mass cuts described in Liu et al. (2018) and Jin et al. (2018) and therefore the mass completeness and homogeneity of the catalog.

In total, out of 4991 sources, we find 21 that we consider to be catastrophic fits ($\chi^2_\nu > 100$); these only make up 0.4% of the entire output catalog and are subsequently removed. The average χ^2 per degree of freedom of the entire data set was computed to be equal to 0.98. The distribution of the FIR properties of the whole sample, their medians, and associated uncertainties are presented in Figure 7 and summarized in Table 1. The catalog containing the extracted FIR properties is described in Appendix A and is publicly available along with the best-fit SED for each object.

We also calculate the position of the galaxies in our sample with respect to the MS, by converting the AGN-free $L_{\text{IR,DL07}}$ estimates to SFR (Kennicutt 1998) and using the functional form of the MS as presented in Schreiber et al. (2015), accounting for

Table 1
Properties of the Galaxy Sample Selected in Section 2

	No. Galaxies	z	$L_{\text{IR,total}}^{\text{a}}$ ($10^{12} L_{\odot}$)	$L_{\text{IR,DL07}}^{\text{b}}$ ($10^{12} L_{\odot}$)	SFR ^c ($M_{\odot} \text{ yr}^{-1}$)	M_{dust} ($10^8 M_{\odot}$)	M_{*} ($10^{10} M_{\odot}$)	f_{AGN} (%)	$\langle U \rangle$
COSMOS	4406	$0.88^{+1.09}_{-0.57}$	$0.45^{+2.17}_{-0.40}$	$0.44^{+2.10}_{-0.39}$	$43.96^{+209.93}_{-38.88}$	$2.73^{+16.66}_{-2.08}$	$4.17^{+5.83}_{-2.89}$	$0.86^{+2.44}_{-0.60}$	$10.12^{+29.55}_{-7.72}$
GOODS-N	585	$1.01^{+1.02}_{-0.53}$	$0.35^{+1.60}_{-0.28}$	$0.34^{+1.53}_{-0.27}$	$33.84^{+152.74}_{-27.02}$	$2.60^{+10.34}_{-1.76}$	$3.56^{+6.03}_{-2.32}$	$2.60^{+4.74}_{-2.14}$	$9.38^{+29.82}_{-6.95}$
All	4991	$0.90^{+1.08}_{-0.58}$	$0.44^{+2.09}_{-0.38}$	$0.42^{+2.04}_{-0.37}$	$42.30^{+203.88}_{-37.06}$	$2.71^{+15.71}_{-2.04}$	$4.07^{+5.93}_{-2.72}$	$0.93^{+3.06}_{-0.67}$	$10.00^{+29.68}_{-7.58}$

Notes. With the exception of redshift and M_{*} , the other quantities are derived via SED fitting. Values are presented as the median and a double-sided 68% confidence interval.

^a Computed over a linear combination of AGN+DL07 best-fit templates.

^b Only considering the best-fit DL07 template.

^c Computed from $L_{\text{IR,DL07}}$.

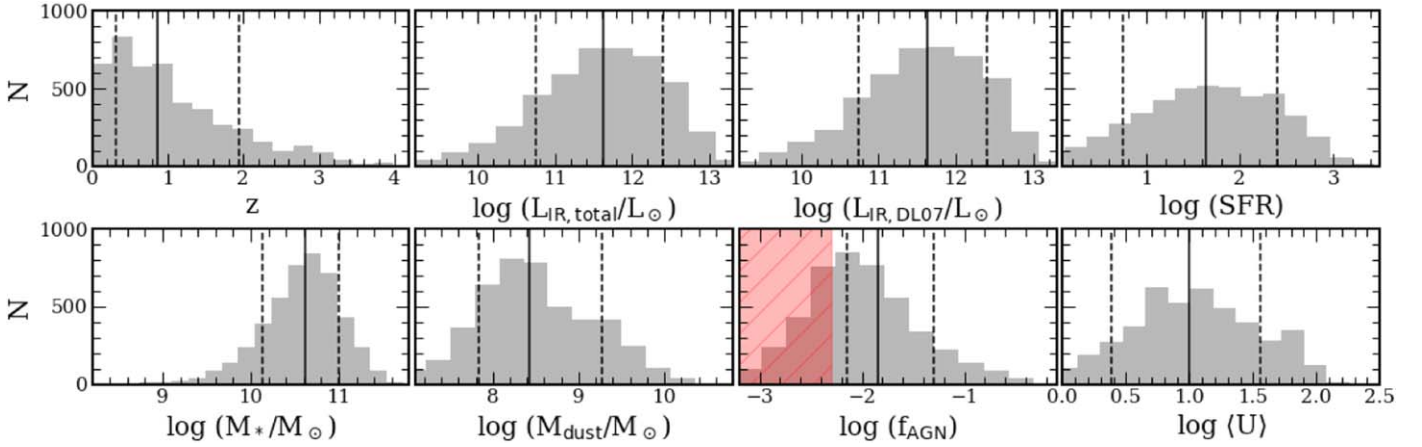


Figure 7. Distribution of the inferred IR properties of the COSMOS and GOODS-N samples. With the exception of z and M_{*} , these properties are the output of our SED fitting code (see Section 3). The black solid and dashed lines represent the median and the 68% confidence interval, respectively. The hatched red region on the f_{AGN} histogram highlights the range where estimates are not reliable (i.e., $f_{\text{AGN}} < 0.005$).

the fact that they use a Salpeter (1955) IMF. The distribution of $\Delta\text{MS} = \text{SFR}/\text{SFR}_{\text{MS}}$ as a function of redshift and stellar mass is presented in Figure 8. We define the boundary between the star-forming and quiescent galaxies at $\log\Delta\text{MS} = -0.5$ dex and between MS and SBs at $\log\Delta\text{MS} = 0.5$ dex, which in linear space corresponds to $\times 3$ below/above the MS. Quite naturally, for decreasing M_{*} and increasing redshift, our sample is progressively restricted to galaxies that lie above the MS. This is shown by the tracks in Figure 8 that indicate the limiting ΔMS for fixed M_{*} as a function of redshift that is reached by our data, after converting the inferred $\text{lim}(L_{\text{IR}})$ to $\text{lim}(\text{SFR})$. Nevertheless, we find that the majority of our sources are classified as MS galaxies (69%), with the remaining objects either considered to be undergoing a phase of “bursty” star formation (26%) or being passive galaxies (5%).

As a final sanity check, we additionally fit the same sources with CIGALE, by utilizing DL07 models and similar sets of optical and AGN templates. We find that the output parameters as derived from the two codes are in good agreement and defer the reader to Appendix C for a more detailed comparison.

5.1. The “ M_{dust} -robust” Sample

We now focus on the FIR properties of the “ M_{dust} -robust” galaxies described in Section 4.1, which should represent the

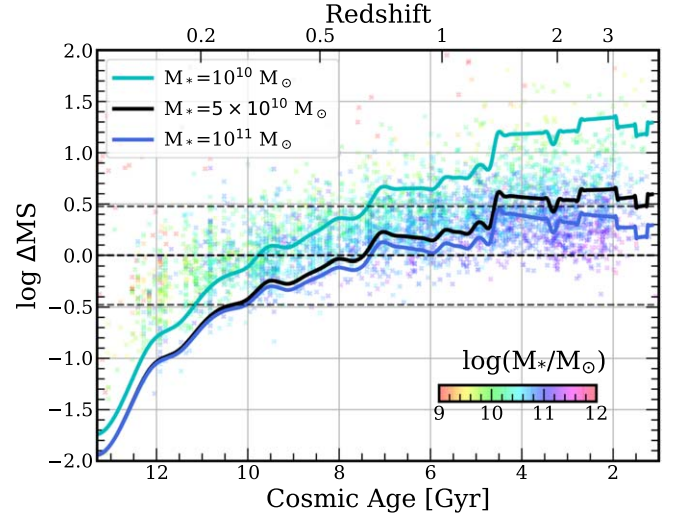


Figure 8. Position of our sources with respect to the MS as a function of cosmic age and redshift. Points are color-coded according to the M_{*} . The dashed black and gray lines denote the MS and its 0.5 dex scatter. The solid colored lines correspond to the ΔMS detection limit as computed based on the inferred $\text{lim}(L_{\text{IR}})$ (see Section 4.2) and assuming $M_{*} = 10^{10}$, 5×10^{10} , and $10^{11} M_{\odot}$.

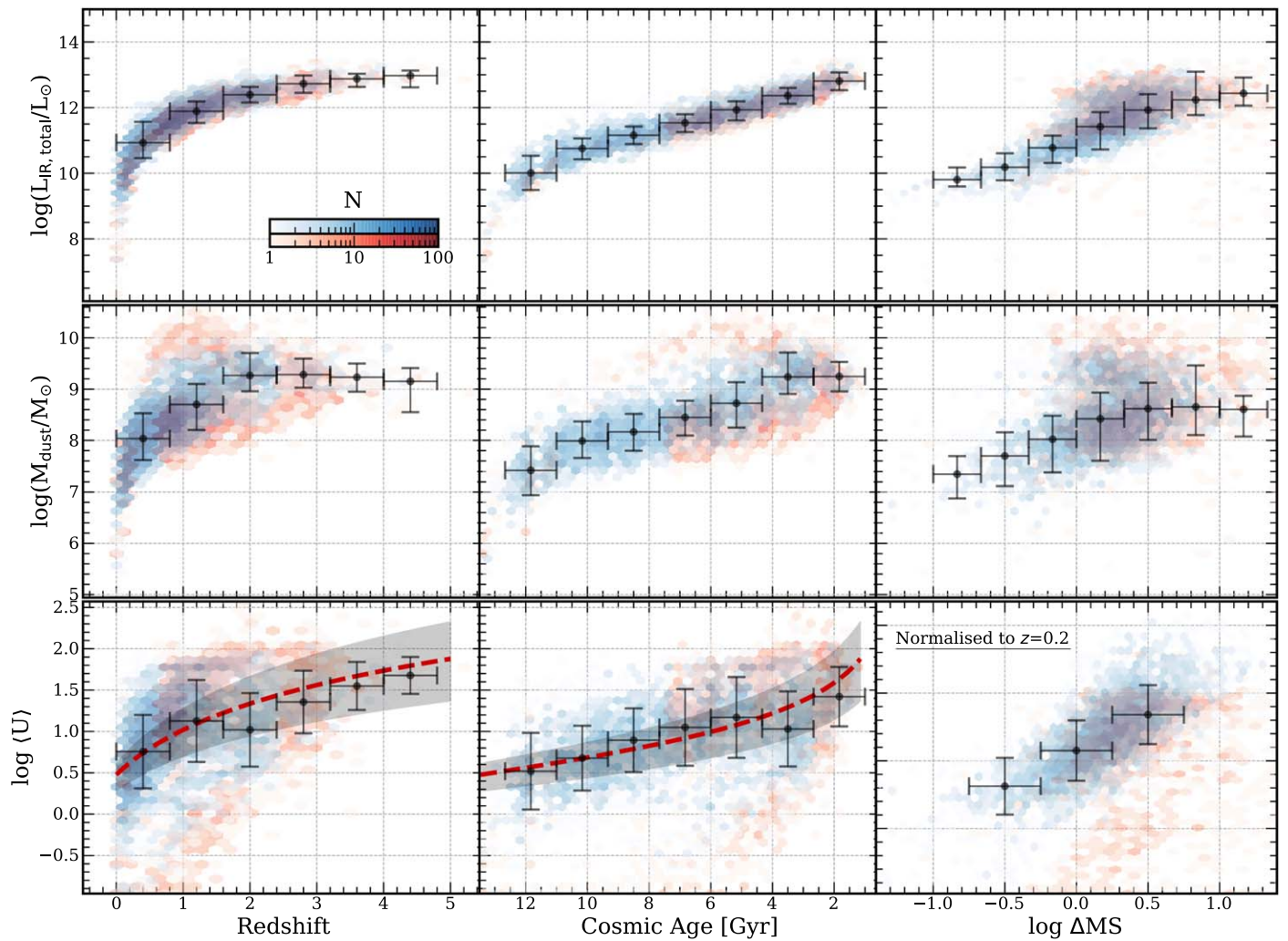


Figure 9. Evolution of general FIR properties, as computed with *Stardust*, as a function of z , cosmic age, and ΔMS . The hexagonal bins are normalized by the number count and contain the “ $M_{\text{dust-robust}}$ ” sample in blue and the objects that were removed after the quality cut in red. For the “ $M_{\text{dust-robust}}$ ” we show the binned median points, with their y -uncertainty corresponding to the 16th and 84th percentile intervals and x -uncertainty corresponding to the bin width. The dashed red lines and shaded regions correspond to the $\langle U \rangle$ - z relation for MS galaxies from Béthermin et al. (2015).

most reliable sample for the exploration of the dependency of the L_{IR} , M_{dust} , and $\langle U \rangle$ on redshift, cosmic age, and ΔMS . The emerging results are presented in Figure 9, where for completeness and to facilitate comparisons we also include the inferred properties of the full sample.

Both L_{IR} and M_{dust} are found to increase smoothly as a function of ΔMS . At the same time, we also find that for MS galaxies $\langle U \rangle$ evolves as $(3.2 \pm 1.3) \times (1 + z)^{1.2 \pm 0.3}$, which is in excellent agreement with the stacking analysis of Béthermin et al. (2015). The fact that our individually detected galaxies appear to follow the same $\langle U \rangle$ - z relation as the much deeper stacked ensembles reinforces the notion that the adopted “ $M_{\text{dust-robust}}$ ” subsample does not introduce a significant bias toward colder objects.

Since $\langle U \rangle$ is proportional to $L_{\text{IR,DL07}}/M_{\text{dust}}$, and also a proxy for T_{d} , our analysis provides further evidence that dust in MS galaxies becomes warmer toward higher redshifts, a trend that has already been recovered in previous studies (most of them based on stacking analysis; see, e.g., Magnelli et al. 2014; Schreiber et al. 2015; Davidzon et al. 2018). Similarly, our data also confirm a

progressive increase of $\langle U \rangle$ (or T_{dust}) with an increasing elevation above the MS (e.g., Magdis et al. 2017; Jin et al. 2019).

It is worth noticing that the full sample follows the same general trends albeit with a considerably larger scatter ($\sim \times 2$) in M_{dust} and $\langle U \rangle$. The reduced scatter for the “ $M_{\text{dust-robust}}$ ” subsample is driven by the imposed $\lambda_{\text{last}} \geq 150 \mu\text{m}$ selection criterion that primarily removes the locus of sources with very cold fitting solutions ($\langle U \rangle \lesssim 1$). We highlight that the rejection of these objects should not introduce a bias in our sample since such low $\langle U \rangle$ values are more indicative of poor photometric coverage/quality (lack of available data point in the R-J) rather than of realistic, extremely cold ISM conditions. However, we note that not all of the extremely cold solutions have been removed from the “ $M_{\text{dust-robust}}$ ” sample by our selection, as ~ 200 objects with $\langle U \rangle < 1$ meet our $\lambda_{\text{last}} > 150 \mu\text{m}$ criterion. These can be easily identified in the $\langle U \rangle$ - z plot and as the outliers populating the secondary blue cloud of points in the $M_{\text{dust}} - \Delta MS$ plot in Figure 9. As we will discuss later, these could be sources with unreliable z_{phot} estimates, failures of the

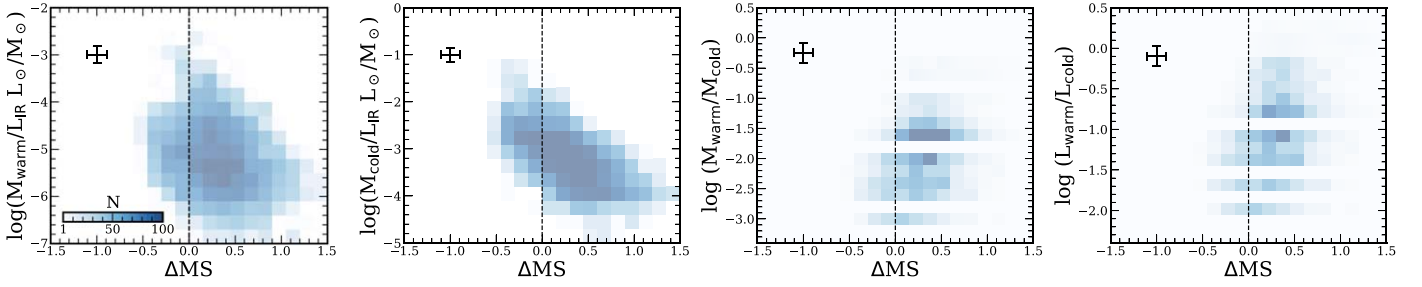


Figure 10. Comparison of the properties of the warm (PDR) and cold (diffuse) dust components of the ISM as a function of ΔMS . From left to right the panels show the warm and cold dust mass components weighted by the total L_{IR} , the fraction of warm to cold M_{dust} , and the fraction of “PDR” to diffuse ISM IR output. The bins are colored based on number density of the data points. We show a typical uncertainty on the plotted parameters in the upper left corner of each panel.

deblending in the SPIRE bands, or, more interestingly, gas giants or very compact galaxies with optically thick FIR emission.

5.2. Cold versus Warm Dust

The SED decomposition introduced in Section 3 can also provide constraints on the relative contribution of the warm (PDR, L_{IR}^{warm} , M_{dust}^{warm}) and cold (diffuse, L_{IR}^{cold} , M_{dust}^{cold}) ISM components to the total L_{IR} output and the total M_{dust} budget of the galaxies in our sample. In particular, it is worth investigating if and how the relative contribution of the components varies as a function of ΔMS . Indeed, if SBs are experiencing elevated star formation activity per surface area (Elbaz et al. 2011, 2018; Valentino et al. 2020), then one would expect to see an increased fraction of L_{IR} (and M_{dust}) originating (and being heated) from the “PDR” component, where the radiation intensity ranges from U_{min} to U_{max} (Draine & Li 2007).

In Figure 10 we plot the inferred properties of the warm and cold ISM components as a function of ΔMS . We find that for a fixed L_{IR} (or equally SFR), SBs tend to have lower amounts of M_{dust}^{cold} , with M_{dust}^{cold}/L_{IR} showing a tight anticorrelation with ΔMS . The same, however, does not apply to M_{dust}^{warm}/L_{IR} , which exhibits a significantly larger scatter and only a very weak dependence on ΔMS . This is a consequence of an increasing fraction of warm to cold M_{dust} and L_{IR} between MS and SB galaxies (Figure 10).

The observed trends suggest that, compared to MS galaxies, SBs have a larger fraction of their total M_{dust} exposed to the intense stellar radiation fields of the PDRs, in agreement with expectations discussed above. Our result could indeed reflect an increase in the compactness of the star formation activity for increasing distance from the MS as suggested in recent high-resolution studies. Finally, under the assumption that M_{dust}^{cold} is proportional to M_{gas} and L_{IR} is proportional to SFR, our results point to enhanced star formation efficiencies and shorter gas depletion timescales for sources residing above the MS, as already reported in the literature (e.g., Daddi et al. 2010; Tacconi et al. 2010, 2020; Magdis et al. 2012a, 2017; Sargent et al. 2014; Silverman et al. 2018).

6. Dust—Stellar Mass Relation and Dust Mass Functions

As discussed in Section 1, constraints on the evolution of f_{dust} and the DMF are key toward a better understanding of dust production and destruction mechanisms at different epochs. Within this context, we explore how the current data set traces the evolution of f_{dust} and use it to characterize the DMFs at various redshifts.

6.1. The Evolution of the Dust Mass Fraction

To infer the evolution of f_{dust} , we adopted the formula described in Liu et al. (2019b), which parametrizes f_{dust} in terms of z , M_* , and ΔMS . Compared to more simple log-space linear fitting models (e.g., Scoville et al. 2017), this formulation recovers trends that are more physically meaningful and also explores how these parameters are covariant and degenerate with each other in a multidimensional fitting space. As an initial check, we performed a Spearman correlation test and found M_{dust} to be mildly correlated with $\log \Delta MS$ ($\rho = 0.40$) and strongly correlated with M_* and t_{age} ($\rho = 0.63$ and -0.80 , respectively). We consider the following functional form:

$$\begin{aligned} \log(f_{dust}) = & (a_0 + a_1 \log(M_*/10^{10}M_\odot)) \log \Delta MS \\ & + b \log(M_*/10^{10}M_\odot) \\ & + (c_0 + c_1 \log(M_*/10^{10}M_\odot)) t_{age}(z) \\ & + d, \end{aligned} \quad (2)$$

where t_{age} is the cosmic age at a given redshift in Gyr and M_* is the stellar mass in M_\odot . For fitting we use the Python package `scipy.optimize.curve_fit`, which finds the solution based on the least-squares method. We also consider how the extreme outliers can affect our results and thus only fit the medians in a given redshift bin. The best-fit values are as follows:

$$\begin{aligned} a_0 = -0.90 & & a_1 = 1.31 \\ b = -0.98 & & c_0 = -0.23 \\ c_1 = 0.11 & & d = -0.64, \end{aligned}$$

with the uncertainties being computed from the covariance matrix. We then used the functional form given by Equation (2) to renormalize all galaxies to lie on the MS ($\Delta MS = 1$) and $M_* = 5 \times 10^{10} M_\odot$, in order to directly compare with our best-fit function in two dimensions.

The normalized data and the best-fit relation presented in Figure 11 are in very good agreement with the collection of similar trends drawn from the literature (e.g., Scoville et al. 2017; Tacconi et al. 2018; Liu et al. 2019b; Magnelli et al. 2020). We note that any apparent discrepancies between the slope and the normalization of our recovered relation to that of Scoville et al. (2017) and Magnelli et al. (2020) are driven by the model parameterization, as for the latter the multivariable functional forms do not consider the covariance between the fitted values.

In Figure 12 we also show how the one-dimensional relation between M_{dust} and M_* compares to the multidimensional fit within six redshift bins. Since our analysis can be affected by the

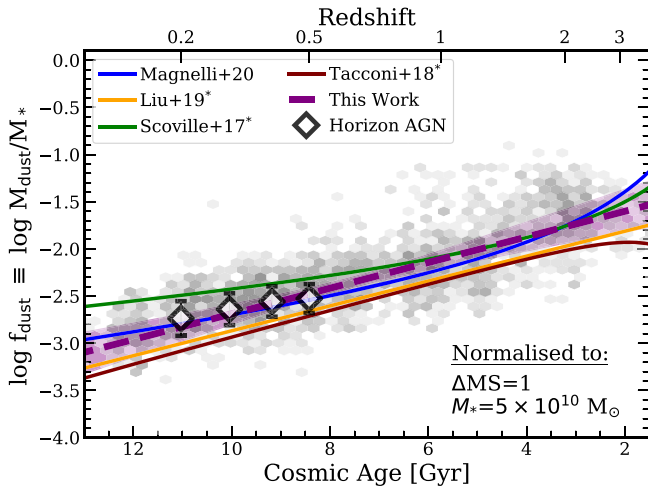


Figure 11. Derived relations for f_{dust} as a function of z/t_{age} . The dashed purple line shows the fit to our data, while solid colored lines display literature results. The shaded purple region denotes the 16th and 84th percentile confidence intervals of our fit. Starred labels denote literature calculations where a direct comparison was not available and a $\delta_{\text{GDR}} = 100$ was assumed. The gray hexbins contain the data from the “ $M_{\text{dust-robust}}$ ” sample and are normalized by the number count. Both the data and the derived relations have been rescaled to $\Delta\text{MS} = 1$ and $M_* = 5 \times 10^{10} M_{\odot}$. White diamonds show median positions of the Horizon-AGN (HAGN) SFGs at that redshift, normalized in the same way as our data.

completeness of our sample in terms of M_* and M_{dust} , we also consider the underlying selection effects based on our $\text{lim}(M_{\text{dust}})(z)$ derivation and assuming that our catalog is complete at $M_* > 10^{10} M_{\odot}$. We find that for a fixed redshift range the inferred $M_{\text{dust}}-M_*$ relation shadows the multiparameter fit up to $z \sim 1.1$, in moderate agreement with the trends reported in Liu et al. (2019b) and Magnelli et al. (2020). However, the increasing incompleteness and the low number statistics do not allow us to extend our analysis at higher redshifts.

Based on these results, we will limit the subsequent DMF analysis to the $0.2 < z < 1.1$ range.

6.2. Dust Mass Functions

After obtaining the functional form for $f_{\text{dust}}(t_{\text{age}}, M_*, \Delta\text{MS})$, we are now in a position to examine the shape and the evolution of the DMF with redshift. For this we will restrict our analysis to the COSMOS sample (SDC2), as we do not have enough statistics or coverage of the GOODS-N field to reliably constrain the DMF.

The “super-deblending” procedure that went into producing the SDC2 catalog creates a significant obstacle when attempting to consider all of the incompleteness effects of the sample. The objects that end up in our sample go through several selection stages, both before and after the deblending procedure. These include both the brightness and mass cuts of the parent catalog (Laigle et al. 2016), the availability of infrared coverage (Jin et al. 2018), and the selection criteria imposed in our study. As such, it is not possible to robustly assess the properties and the number of objects that end up being “lost.” Therefore, we select an alternative approach in computing the DMF for our objects, namely, utilizing the derived f_{dust} parameterization along with the available SMFs in the literature. Later in this section, we also attempt to account for the incompleteness effects and compare the SMF-derived DMF to the observed number density of galaxies per M_{dust} bin.

6.2.1. DMF from SMF

For our analysis we adopt the SMF computed by Davidzon et al. (2017), which covers the entire COSMOS field and the $z = 0.2-4$ range. Their mass function already accounts for the Eddington bias, so we do not need to consider any additional corrections. Since the vast majority of galaxies in our sample are star-forming, we adopt the derived parameters for the “active” SMF only.

The galaxy mass function is normally expressed as a Schechter function (Schechter 1976), which in logarithmic form can be written as

$$\Phi(\log M)d(\log M) = \ln(10) \exp(-M/M^*) \times \Phi^*(-M/M^*)^{(\alpha+1)} d(\log M_*), \quad (3)$$

where α is the slope of the faint end, Φ^* is the normalization, and M^* is the characteristic mass, indicating the position of the “knee” of the Schechter function. To convert the SMF to DMF, we first postulate that the number of galaxies in a given redshift bin is the same, regardless of whether we integrate over M_* or M_{dust} , namely,

$$\int_0^{\infty} \Phi(\log M_*)d(\log M_*) = \int_0^{\infty} \Phi(\log M_{\text{dust}})d(\log M_{\text{dust}}),$$

and the integrands can be rearranged to obtain

$$\Phi(\log M_{\text{dust}}) = \Phi(\log M_*)d(\log M_*)/d(\log M_{\text{dust}}).$$

We then differentiate Equation (2), to obtain $d(\log M_*)/d(\log M_{\text{dust}}) = (b + c_1 \times t_{\text{age}} + 1)^{-1}$. In order to perform the final conversion, we also transform all the M_* bins into M_{dust} bins, by inverting our formulation of f_{dust} , taken at $\Delta\text{MS} = 1$.

6.2.2. Accounting for the Eddington Bias

Before comparing to the real data, it is important to note that, while calculating the SMF-derived DMF, the Eddington bias, induced by the f_{dust} scatter, should be taken into account. Since we are directly employing the Davidzon et al. SMF, where the Eddington bias has already been corrected, using the best-fit f_{dust} relation to convert SMF to DMF will only reproduce the median trend and will not properly account for the full dynamic range of observed M_{dust} . To alleviate this, we rely on the work by Loveday et al. (1992), which showed that the Eddington bias manifests itself as a Gaussian, whose width is equal to the scatter of the variable of interest, convolved to the mass function. We have thus utilized an approach similar to that used in Davidzon et al. (2017) for the SMF and in Beeston et al. (2018) for the DMF, where they successfully deconvolve their observed mass functions by using the scatter of the observed variable. As such, within each redshift bin we consider the standard deviation of the f_{dust} in a logarithmic space. We then use this scatter to create a simple Gaussian that is centered at zero, and then we convolve it with our SMF-derived DMF. This allows us to better take into account the scatter of our data and thus produce a more realistic mass function. In conclusion, we have indirectly produced two versions of SMF-derived DMFs, with and without the scatter.

6.2.3. Comparison to the Observed Number Density

Now we would like to compare the SMF-derived DMF to the observed number density of galaxies in the “ $M_{\text{dust-robust}}$ ” sample. To this end, we first apply the widely used nonparametric

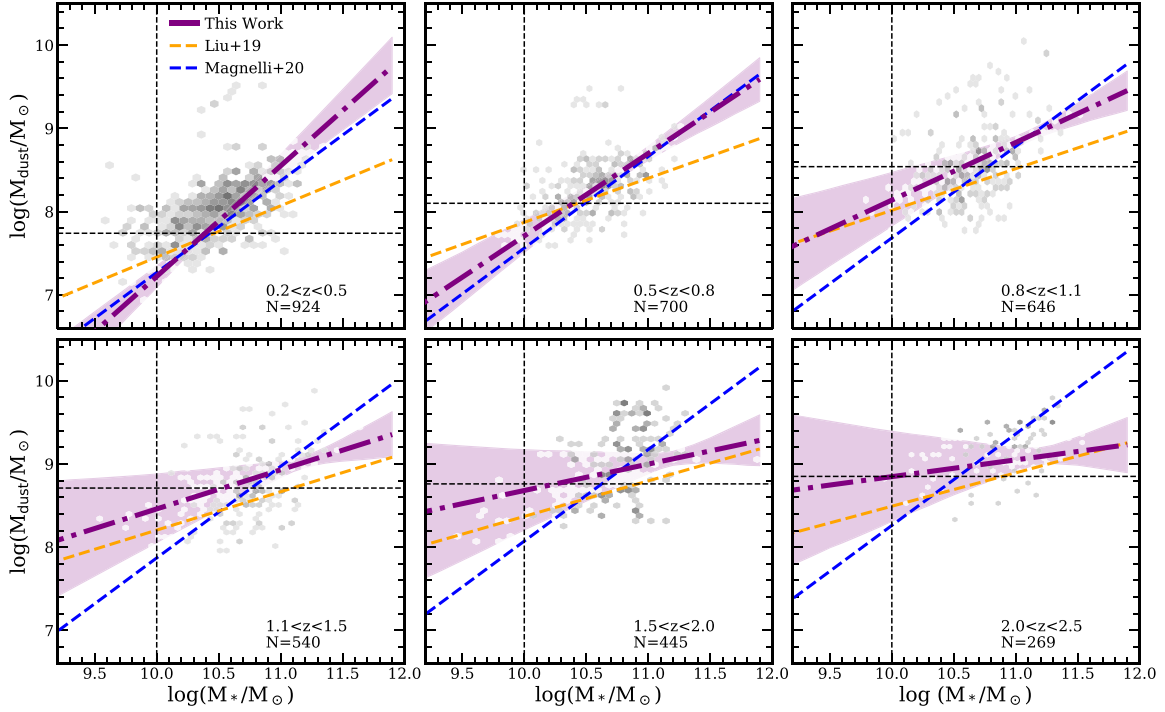


Figure 12. M_{dust} as a function of M_* in six redshift bins. The dashed–dotted purple line represents our best fit from Equation (2) that was collapsed to a single dimension, with $\Delta\text{MS} = 1$ and $z = \langle z_{\text{bin}} \rangle$. The shaded purple regions denote the 16th and 84th percentile confidence intervals of our fit. The orange and blue lines show the relations derived in Liu et al. (2019b) and Magnelli et al. (2020), respectively. The dashed black lines represent the detection limits of the original catalog, in M_* (vertical), and the $\text{lim}(M_{\text{dust}})$ that we compute in Section 4.2 (horizontal).

$1/V_{\text{max}}$ method to correct for the Malmquist bias of our sample (Schmidt 1968). This method relies on assigning the V_{max} to each redshift bin, based on the detection limits of the survey. Effectively, this correction accounts for the fact that in a given volume a brightness-limited survey is more likely to pick up the bright sources, while missing faint galaxies, which would populate the low- M_{dust} end. We explicitly highlight that the V_{max} correction only accounts for the FIR flux rms cuts and not the selection criteria outlined in Section 2.3.

To calculate the V_{max} , we use the prescription from Weigel et al. (2016), which provides a volume correction for each individual source. As a first step, and for a given redshift bin, we split our sources into 0.4 dex bins in the $\log(M_{\text{dust}}/M_{\odot}) = 6\text{--}11$ interval. Given that the median uncertainty on the M_{dust} is ~ 0.3 dex, the following bin spacing will ensure that there is very little to no cross-contamination between mass bins. The $V_{\text{max}, i}$, where i denotes an individual galaxy, can be then calculated as

$$V_{\text{max}} = \frac{A}{3} (d_c(z_{\text{max},i})^3 - d_c(z_{\text{min},i})^3), \quad (4)$$

where d_c is the comoving distance and A is the area, which in our case is equal to 1.38 deg^2 . Following Weigel et al. (2016), the $z_{\text{min},i}$ is given simply by the lower boundary of the bin. The $z_{\text{max},i}$, on the other hand, can be calculated empirically, either through detection limits of individual bands or by considering a limiting mass of the survey. It, however, cannot exceed the maximum redshift of the bin.

To obtain the z_{max} , we consider the best-fit SEDs for our sources and the rms of the parent catalogs in order to redshift the sources to the point where they no longer fulfill our selection criteria as outlined in Section 2. Using this method, we, however, found that, for an overwhelming majority of

sources, the computed $z_{\text{max},i}$ exceeds the upper boundary of the bin they belong to. Therefore, the V_{max} correction that we apply becomes effectively bound between the lower and the upper redshift of the bin. We find that this method works best in the lowest ($0.2 < z < 0.5$) redshift bin, with the $\langle V/V_{\text{max}} \rangle$ test returning a value of 0.47. The remaining two redshift bins are significantly incomplete, with the ratio returning 0.83 and 1.38, respectively.

Among the other sources of incompleteness, as discussed in Section 6.2, here we can attempt to account for lost sources due to the sensitivity limits of the survey and failures in the deblending procedure. We therefore multiply our points by the loss fraction in each redshift bin that is computed as the ratio between sources in our catalog over the sources that have $\text{SN-IR} > 1$ in the parent catalog.²¹ The SN-IR parameter, described in greater detail in Liu et al. (2018) and Jin et al. (2018) and references therein, considers a combination of FIR bands starting with $100 \mu\text{m}$. We thus expect that in this context our SN-IR threshold can indicate whether a galaxy is intrinsically dusty.

The comparison of the SMF-derived DMF with and without the Eddington bias taken into account, along with the observed volume-weighted number density of galaxies, derived as described above, for three redshift bins, is presented in Figure 13. We find that the DMF without the Eddington bias is insufficient to reproduce the observed dynamic range of M_{dust} , particularly in the higher-redshift bins, exactly as we have predicted in Section 6.2.2. On the other hand, the SMF-derived DMF with the artificially induced bias, through the f_{dust} scatter, is in good agreement with the data in the high-mass

²¹ $\text{SN-IR}^2 = \sum_{\lambda} (S/N)_{\lambda}^2$, with $\lambda \geq 100 \mu\text{m}$.

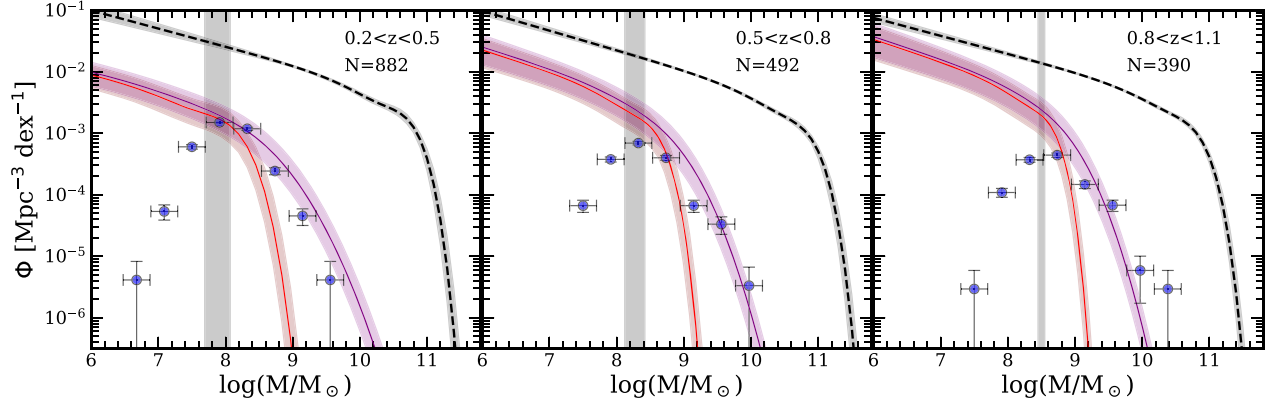


Figure 13. Derived DMFs in the $0.2 < z < 0.5$, $0.5 < z < 0.8$, and $0.8 < z < 1.1$ ranges. The dashed black line represents the original SMF for active galaxies from Davidzon et al. (2017). The purple and red lines are the DMFs obtained by converting the SMF, with and without the Eddington bias applied, respectively. The blue points are the DMF calculated directly from our data. The shaded rectangular area highlights the theoretical prediction for $\text{lim}(M_{\text{dust}})$ in that redshift interval.

end, further highlighting the necessity of accounting for the observational biases when inferring relations (i.e., $M_{*}-M_{\text{dust}}$ in our case) through the observed mass (or luminosity) functions. Although our model underpredicts the high-mass end data in the higher-redshift bin, both still agree within the error bars. At the same time, though, in the low-mass regime our data significantly underestimate the number density of galaxies mirroring the incompleteness of our sample in this M_{dust} regime. It is worth noticing, though, that the turnover of the observed data perfectly coincides with the independent estimates of $\text{lim}(M_{\text{dust}})$, offering an indirect validation of our simulations presented in Section 4.2. For the analysis in the next sections, we adopt the SMF-derived DMF, which has the Eddington bias corrected out, as the final result against which we will compare previous observationally driven DMFs and theoretical predictions.²²

7. Gas Content of Star-forming Galaxies

The inferred M_{dust} estimates can be used as an invaluable proxy of the gas mass (M_{gas}). To this end, we adopt the metallicity-dependent gas-to-dust mass ratio δ_{GDR} technique, which takes advantage of the relatively tight anticorrelation between the gas-phase metallicity and the δ_{GDR} of galaxies, both in the local universe and at high z (see, e.g., Leroy et al. 2011; Magdis et al. 2012a; Rémy-Ruyer et al. 2014; Genzel et al. 2015). For a source with known metallicity (Z) and M_{dust} , one can estimate the amount of M_{gas} via the following relation:

$$M_{\text{gas}} = \delta_{\text{GDR}}(Z)M_{\text{dust}}, \quad (5)$$

where M_{gas} corresponds to $M_{\text{H}_2} + M_{\text{HI}}$, i.e., the sum of the atomic and molecular hydrogen.

Given the absence of direct metallicity measurements for our sample, we adopt the fundamental metallicity relation (FMR) of Mannucci et al. (2010). In particular, we use the M_{*} and SFR estimates as inputs to the FMR and obtain metallicities calibrated for the Kewley & Dopita (2002; KD02) photo-ionization models. These metallicities are subsequently converted to the Pettini & Pagel (2004; PP04 N2) scale following Kewley & Ellison (2008). We then estimate the δ_{GDR} of each galaxy through the $\delta_{\text{GDR}}-Z$ relation of Magdis et al. (2012a),

given as

$$\log(\delta_{\text{GDR}}) = (10.54 \pm 1.00) - [12 + \log(\text{O}/\text{H})]^{(0.99 \pm 0.12)}, \quad (6)$$

and subsequently derive M_{gas} through Equation (5), for all the sources in SDC1 and SDC2 catalogs. We propagate the uncertainties on M_{gas} by taking into account the uncertainty on M_{dust} and combining it with the typical scatter of 0.2 dex on the $\delta_{\text{GDR}}-Z$ relation (Magdis et al. 2012b). These inferred M_{gas} estimates with associated uncertainties are included in the released catalog.

7.1. Gas–Stellar Mass Relation

Similarly to f_{dust} , we also explore the dependence of f_{gas} on cosmic age, ΔMS , and M_{*} . We utilize the same multiparameter fitting function as before (see Equation (2)) and focus on the “ $M_{\text{dust}}\text{-robust}$ ” sample. We calculate the Spearman rank correlation between our variables and find M_{gas} to be mildly correlated with $\log\Delta\text{MS}$ and M_{*} ($\rho = 0.47$ and 0.53 , respectively) and strongly negatively correlated with t_{age} ($\rho = -0.82$). The fitting procedure yields the following best-fit parameters:

$$\begin{aligned} a_0 &= -0.73 & a_1 &= 1.16 \\ b &= -1.02 & c_0 &= -0.20 \\ c_1 &= 0.09 & d &= 1.39. \end{aligned}$$

The best-fit $f_{\text{dust}}-t_{\text{age}}$ (or redshift) relation and our data, both normalized to $\Delta\text{MS} = 1$ and $M_{*} = 5 \times 10^{10} M_{\odot}$, are presented in Figure 14 (top). Similar to previous studies (Scoville et al. 2017; Tacconi et al. 2018; Liu et al. 2019b; Magnelli et al. 2020), we find a sharp increase in the gas fraction up to $z = 2$, followed by a milder evolution at higher redshifts, a change that is noticeable only in the $f_{\text{dust}}-z$ parameter space. We note, however, that due to poor statistics and lack of spectroscopic redshifts, our data cannot reliably constrain the high- z evolution of f_{gas} at $z > 2$. We also detect a population of sources that display significantly elevated gas reservoirs for their redshift ($\log(f_{\text{gas}}) > 0.5$). Some of those objects either have only a z_{phot} estimate available or appear to be blended in the SPIRE bands and therefore could have an erroneously large M_{dust} and subsequently M_{gas} estimate assigned to them. However, among these, we do identify some sources with spectroscopic redshifts, which are also “clean”/isolated in the IR maps. In particular, we

²² Tables containing the DMFs can be accessed at https://github.com/VasilyKokorev/sdc_ir_properties.

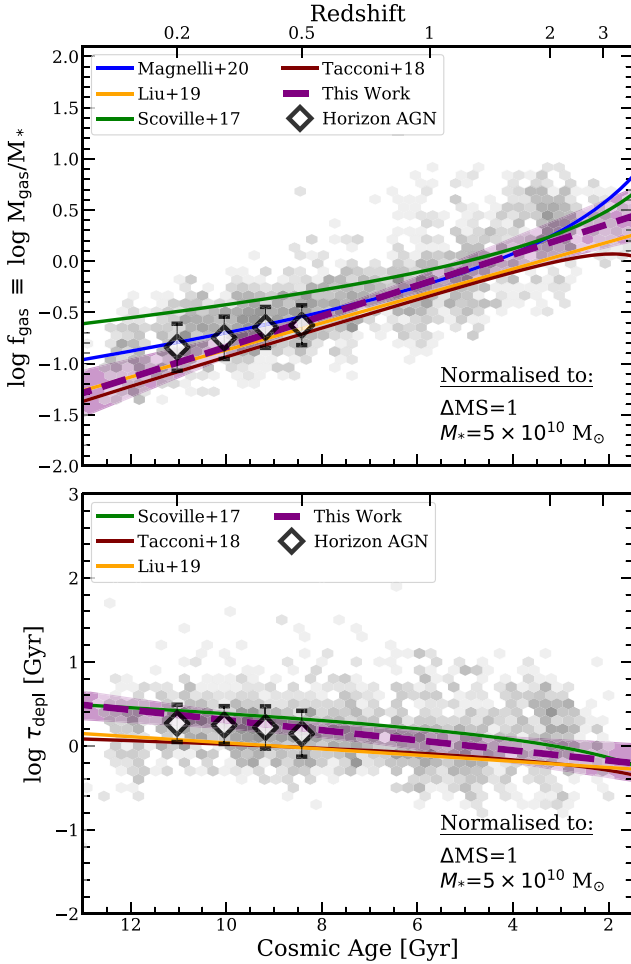


Figure 14. Derived relations for f_{gas} (top) and τ_{depl} (bottom) as a function of z/t_{age} . The dashed purple line shows the fit to our data, while solid colored lines display literature results. The shaded purple region denotes the 16th and 84th percentile confidence intervals of our fit. The gray hexbins contain the data from the “ $M_{\text{dust-robust}}$ ” sample and are normalized by the number count. Both the data and the derived relations have been rescaled to $\Delta\text{MS}=1$ and $M_* = 5 \times 10^{10} M_{\odot}$. White diamonds show median positions of the HAGN SFGs at that redshift, normalized in the same way as our data.

find ~ 40 such sources with $\log(f_{\text{gas}}) > 0.5$) and six with $\log(f_{\text{gas}}) > 1$ that, as we discuss later, we coin as “gas giants.”

7.2. Evolution of Depletion Time

Finally, we focus our attention on the depletion time $\tau_{\text{depl}} = M_{\text{gas}}/\text{SFR} = 1/\text{SFE}$. We employ the same fitting technique as before and explore the evolution of τ_{depl} with cosmic age, ΔMS , and M_* in a multidimensional parameter space, for the “ $M_{\text{dust-robust}}$ ” sample. The τ_{depl} correlates mildly with age and ΔMS (Spearman $\rho = -0.46$ and -0.58 , respectively) and weakly with M_* ($\rho = -0.23$). The best-fit parameters are as follows:

$$\begin{aligned} a_0 &= -1.65 & a_1 &= 1.42 \\ b &= -0.95 & c_0 &= -0.02 \\ c_1 &= 0.12 & d &= 0.37. \end{aligned}$$

We show the best-fit $\tau_{\text{depl}}-t_{\text{age}}$ relation and our data, both normalized to $\Delta\text{MS} = 1$ and $M_* = 5 \times 10^{10} M_{\odot}$, in Figure 14 (bottom). In line with the previous studies of

τ_{depl} by Scoville et al. (2017), Tacconi et al. (2018), and Liu et al. (2019b), we recover a relatively weak decrease of depletion time (or increase in SFE) with redshift.

8. Discussion

8.1. On the Dust and Gas Scaling Relations

The recovered trends between M_{dust} , M_* , and M_{gas} and their evolution with redshift offer a test bed against which theoretical and previous observationally driven studies can be compared to. As shown in Figures 11 and 14, our analysis yields f_{dust} and f_{gas} evolutionary tracks consistent with those presented in Tacconi et al. (2018), Liu et al. (2019b), and to a smaller degree those reported in Scoville et al. (2017) and Magnelli et al. (2020). As discussed earlier, the mild tension between the latter works and our results could be primarily attributed to the choice of the fitting function.

The f_{dust} and f_{gas} in our sample of SFGs increase rapidly from $z = 0$ to $z = 1$, peak around $z \sim 2-3$, and then remain roughly constant. It is, however, a point of contention whether the latter is driven by actual physical processes or is a consequence of the scarcity of data at $z > 2$. It is also worth mentioning that our analysis points toward a milder evolution of f_{dust} (-0.8 dex) compared to f_{gas} (-1.3 dex) from $z = 2$ to $z = 0$, with the latter dropping $\sim 3 \times$ faster. This is aligned with the evolution of ρ_{dust} and ρ_{gas} derived by the ALMA stacking analysis of Magnelli et al. (2020) and could in fact reflect the evolution of metallicity, and thus of δ_{GDR} , for fixed M_* toward lower redshifts.

At the same time, the decrease of M_{dust} with decreasing redshift, for fixed M_* , can be attributed to either the destruction of dust grains by interstellar radiation fields or their incorporation into the stellar population. This is discussed in more detail in Donevski et al. (2020), who also report a decreasing f_{dust} from earlier cosmic age to the present epoch. We note that the observed trend could also mirror the overall decline in the SFR density in the universe from $z = 2$ to the present day, which points toward lower star formation activity and thus lower dust production at later cosmic epochs. Finally, at a fixed redshift, both f_{dust} and f_{gas} decrease as a function of M_* (as indicated by a negative value of the fitting parameter b ; see Equation (2)), in line with previous studies (e.g., Magdis et al. 2012a; Magnelli et al. 2020 and references therein).

In addition to observational studies, we can also compare our results to theoretical predictions. To this end, we consider the HAGN hydrodynamical simulations in the COSMOS field (Dubois et al. 2014; Laigle et al. 2019) and draw a sample of SFGs ($\Delta\text{MS} > 0.3$) in the $z = 0.2-0.5$ range, selected to meet the M_* completeness of the COSMOS 2015 survey, and which fall within a simulation box of 143 Mpc per side (Dubois et al. 2014). To measure ΔMS for each galaxy, we considered the M_* and the 100 Myr averaged SFR from the simulations. Also, since M_{dust} is not an explicit parameter of HAGN galaxies, we used a constant $\delta_{\text{GDR}} = 100$ to convert the M_{gas} values, as derived from the simulations, to M_{dust} . We then use the M_{gas} , M_* , and M_{dust} of the simulated galaxies to infer f_{gas} and f_{dust} . The median values and their scatter, renormalized to $\text{MS} (\Delta\text{MS} = 1)$ and $M_* = 5 \times 10^{10} M_{\odot}$ in four redshift bins, are presented and compared to the real data in Figures 11 and 14. We find a good agreement between the theoretical predictions and our observationally driven trends (in the $0.2 < z < 0.5$ range at least), indicating that the HAGN simulation can successfully reproduce the baryonic

components of the galaxies and its evolution with redshift. Conversely, the agreement of our results with both theoretical and observational studies provides an extra indirect validation for the performance of our new SED fitting code.

8.2. On the Evolution of Depletion Time

As with f_{dust} and f_{gas} , our recovered trends, which connect τ_{depl} to redshift, ΔMS , and M_* , show similar behavior to the ones presented in Scoville et al. (2017), and to a lesser extent those in Tacconi et al. (2018) and Liu et al. (2019b). The dependence of τ_{depl} on M_* is relatively weak across all studies; however, similarly to Liu et al., we find that the depletion time for high-mass galaxies increases from early cosmic ages toward present times, while low-mass galaxies display an opposite trend of decreasing τ_{depl} with cosmic age. As discussed in Liu et al. (2019b) and Hodge & da Cunha (2020), this could be a signature of downsizing, meaning that more massive galaxies evolve at earlier times.

During our analysis, we find $\tau_{\text{depl}} \sim (1+z)^{-1.07}$, which is more reflective of the scaling relations derived in Scoville et al. (2017) ($\tau_{\text{depl}} \sim (1+z)^{-1.04}$), rather than weaker dependencies ($\tau_{\text{depl}} \sim (1+z)^{-0.62}$ and $(1+z)^{-0.58}$) found by Tacconi et al. (2018) and Liu et al. (2019b), respectively. As expected, and in line with the literature results, we also find that galaxies above the MS (at a fixed M_* and z) form stars with a much higher efficiency (lower τ_{depl}) than their MS counterparts, with $\tau_{\text{depl}} \sim \Delta\text{MS}^{-1.68}$. We would also like to caution the reader and highlight the fact that Tacconi et al. and Scoville et al. use functional forms that are different from ours, when fitting for evolution of τ_{depl} . For example, Tacconi et al. consider additional dependence on the effective radius R_e , which might inadvertently carry some redshift dependence. As such, the fitted exponents are not necessarily directly comparable. The differences between evolutionary trends could also be attributed to the different samples used (see, e.g., Hodge & da Cunha 2020).

Presumably, the existence of these outliers can be explained by an increased SFE, which results from major-merger events (see, e.g., Scoville et al. 2017; Cibinel et al. 2019). In fact, galaxies that lie above the MS are also found to have increased gas fractions (Dekel et al. 2009; Tacconi et al. 2020), which is attributed to a more efficient gas accretion from the cosmic web, but the enhanced gas reservoirs are still not large enough to explain significantly enhanced sSFR. The debates regarding the exact reason, which results in an onset of an SB-like mode of star formation, are still ongoing; however, it seems very likely that it is a combination of both increased gas fractions and enhanced SFE. We find that our sample supports this notion, with galaxies above the MS having both large gas reservoirs with median $\log(f_{\text{gas}}) = 0.15$, meaning that gas mass reservoirs take up $\sim 59\%$ of the total baryonic matter, and relatively short depletion times of ~ 400 Myr. Our M_{gas} values were, however, derived with a general FMR, assuming solar-like metallicities. This, however, might not be applicable for SBs, which can display elevated metallicities owing to the increased sSFR. In fact, it has been shown (see, e.g., Silverman et al. 2015) that if SBs had supersolar metallicities, it would drive down δ_{GDR} , together with f_{gas} , and in turn result in increased SFE, thus implying that only the SFE is responsible for galaxies being elevated above the MS.

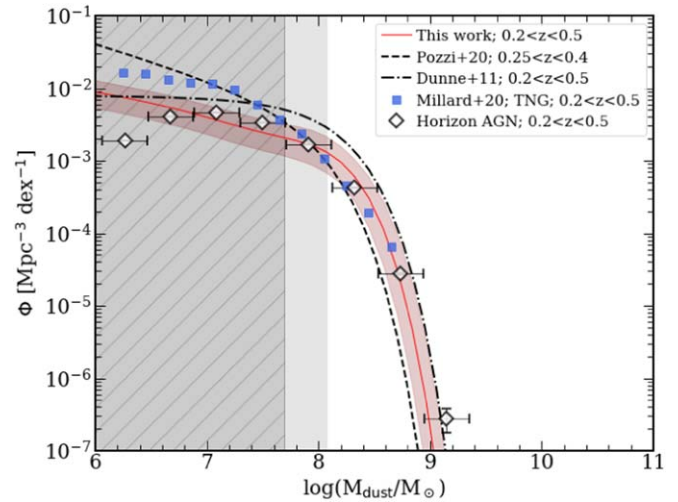


Figure 15. A compilation of the theoretical and observationally derived DMFs in the $0.2 < z < 0.5$ range. The Davidzon et al. (2017) SMF, converted to DMF, is shown as the solid red line, with the shaded area corresponding to the 1σ uncertainty. The dashed and dashed-dotted black lines correspond to the DMFs of Pozzi et al. (2020) and Dunne et al. (2011), respectively, rescaled to $\kappa_{250\ \mu\text{m}} = 0.51\ \text{m}^2\ \text{kg}^{-1}$. The white diamonds and the blue squares depict the theoretical predictions of the HAGN and TNG simulations from Dubois et al. (2014) and Millard et al. (2020), respectively. The gray shaded region highlights the M_{dust} regime below the $\text{lim}(M_{\text{dust}})$ of our sample, as derived in Figure 6. The hatched region denotes the M_{dust} regime where our sample becomes severely limited, i.e., $>1\sigma$ below $\text{lim}(M_{\text{dust}})$.

8.3. On the DMFs and the Theoretical Predictions

With the derived DMF in hand, we are also in position to bring together our findings with those presented in previous observationally driven studies and provide a direct comparison to the theoretical predictions as inferred by recent simulations. For our purposes, we focus on the $0.2 < z < 0.5$ redshift interval that contains the majority of our objects and offers the most robust statistical analysis. These results are shown in Figure 15.

We first compare our DMF to that presented in Pozzi et al. (2020), based on a PACS $160\ \mu\text{m}$ selected sample of SFGs. In Figure 15, the two DMFs appear to be in tension in both the high- and low-mass ends, with our compilation overpredicting the number density of galaxies with high M_{dust} and underpredicting that of less dusty sources. The discrepancy between the two DMFs can be attributed to the choice of fitting methods/templates, the adopted κ_ν to infer M_{dust} , and selection effects. For example, the DL07 templates adopt a $\kappa_{250\ \mu\text{m}}$ of $0.51\ \text{m}^2\ \text{kg}^{-1}$, while the analysis in Pozzi et al. uses $\kappa_{250\ \mu\text{m}} = 0.4\ \text{m}^2\ \text{kg}^{-1}$, which would result in 0.1 dex smaller M_{dust} estimates. It is also important to point out that Pozzi et al. compared their modified blackbody (MBB) SED fitting to MAGPHYS, finding that their MBB method recovers systematically lower M_{dust} . Indeed, the choice of the fitting methodology can induce up to a factor of two difference in derived M_{dust} (see, e.g., Magdis et al. 2013 and an in-depth comparison in Berta et al. 2016). Moreover, for a flux-limited survey, the mere selection at $\lambda_{\text{obs}} = 160\ \mu\text{m}$ could introduce a bias toward warmer sources that for fixed L_{IR} have lower M_{dust} and that could explain the small number density of sources with $\log(M_{\text{dust}}/M_\odot) > 8$. While it is not possible to correct for the effects of selection and broader SED fitting methodology, we have rescaled the Pozzi et al. DMF to have the same $\kappa_{250\ \mu\text{m}}$ as was adopted in our analysis.

We also compare our results to Dunne et al. (2011), who computed a DMF based on a sample of 250 μm selected galaxies. For our comparison, we have rescaled their DMF by -0.24 dex, to account for the difference in κ_{ν} . Contrary to Pozzi et al. (2020), we now find that Dunne et al. (2011) overpredict the number density of dusty galaxies at high dust masses. This again can be understood in terms of selection effects since the 250 μm selection could bias the sample toward cold sources and thus to higher M_{dust} values (again, for a flux-limited survey). While our criterion for at least one detection at $\lambda_{\text{rest}} > 150 \mu\text{m}$ could be perceived as similar to a 250 μm selection at $z \sim 0.3$, we note that the requirement for two extra detections at $\lambda_{\text{rest}} < 150 \mu\text{m}$ and the super-deblended catalogs, which allow for the detection of fainter than the nominal confusion noise in the SPIRE bands, ease any bias toward either intrinsically cold or warm objects. This is further supported by the fact that our SMF-derived DMF, where the Eddington bias has already been corrected, falls directly between the calculations from Pozzi et al. and Dunne et al. (Figure 15). In conjunction with the derivation of a $\langle U \rangle - z$ relation that is in excellent agreement with the stacking analysis of Béthermin et al. (2015), this suggests that the careful treatment of selection criteria and of the detection limits of our parent sample has allowed us to gain a unique and unbiased perspective on the evolution of dust properties of COSMOS galaxies.

Finally, we compliment our analysis by comparing our DMF to the theoretical predictions of the HAGN and IllustrisTNG simulations (Millard et al. 2020). In order to produce an HAGN DMF, we define a simulated sample following the procedure described above, bin the galaxies in 0.4 dex intervals of M_{dust} , and normalize by the volume of the simulation ($4 \times (142)^3 \text{ Mpc}^3$). For the IllustrisTNG simulation, Millard et al. (2020) consider multiple TNG100 snapshots in a box size of 106 Mpc per side, comparable to the HAGN simulated subset presented earlier. The TNG-DMF is constructed through the M_{dust} values of the simulated galaxies, derived in post-processing through a fixed dust-to-metals ratio of 0.5.

Unlike real data, simulations do not suffer from observational bias and as such should be compared to DMF derived from the SMF, without adding the Eddington bias. As shown in Figure 15, both HAGN and IllustrisTNG are in excellent agreement with the high-mass end of our SMF-derived DMF. Notably, the HAGN DMF is also consistent with our results at the low-mass end down to $M_{\text{dust}} \sim 10^7 M_{\odot}$. We recall that, for simplicity, when converting M_{gas} to M_{dust} for the HAGN sample, we considered a universal $\delta_{\text{GDR}} = 100$. However, for sources with lower M_* ($< 10^8 M_{\odot}$) and thus with subsolar metallicities, a larger δ_{DGR} (~ 150) is probably more applicable (Rémy-Ruyer et al. 2014). This would translate into a $\times 1.5$ downward correction for the low-mass HAGN bins, bringing them into exact agreement with our DMF down to $M_{\text{dust}} \approx 10^7 M_{\odot}$. We note that this M_{dust} , assuming an average $M_{\text{gas}}/M_{\text{dust}} \approx 100$, corresponds to the M_* completeness limit of the simulation ($M_* \approx 10^9 M_{\odot}$). Therefore, the observed decline of the number density of the HAGN galaxies at $M_{\text{dust}} \leq 10^7 M_{\odot}$ is fully consistent with the expectations.

In comparison to the TNG-DMF, though, we predict a factor of 2.5 fewer objects at the low-mass end. This tension could arise from the incompleteness of our sample at the low-mass end, which leaves the slope of the $M_{\text{dust}} - M_*$ relation at $M_{\text{dust}} < 5 \times 10^7 M_{\odot}$ largely unconstrained. We are thus unable

to ascertain whether this discrepancy is caused by the limitations of our sample, or whether the TNG simulations overpredict the number density of the galaxies in the low-mass end.

Put together, these comparisons indicate that, at least down to $M_{\text{dust}} \approx 5 \times 10^7 M_{\odot}$, our $M_{\text{dust}} - M_* - z$ relation and the resulting DMFs are robust and fully consistent with the theoretical expectations.

8.4. Population of Gas Giants

As briefly discussed in Section 7, during our analysis we identified some extreme outliers from the average f_{dust} and f_{gas} evolutionary trends (Figures 11 and 14), which typically have $\log(f_{\text{gas}}) > 0.5$, i.e., their gas mass reservoir takes $\sim 75\%$ of their baryonic matter. Since z_{phot} could be a major source of uncertainty in both M_* and M_{gas} , before looking further into this population of “gas giants,” we first narrow down our sample to spectroscopically confirmed sources. We then examined the individual SEDs and the cutout images of the remaining sources in order to identify either poor coverage of the FIR peak or blending issues that could result in erroneously large M_{gas} estimates. With the above considerations, we are left with 41 objects whose extreme f_{gas} can only be explained by gigantic M_{gas} reservoirs. This population spans a wide range in redshift ($0.21 < z < 4.05$, $\langle z \rangle = 1.34$), with $9.0 < \log(M_*/M_{\odot}) < 11.3$, $\langle \log(M_*/M_{\odot}) \rangle = 10.3$ and $0.11 < \Delta\text{MS} < 14.2$, $\langle \Delta\text{MS} \rangle = 1.8$. The best-fit SEDs of two such objects are presented in Figure 16. We also note that these two sources are otherwise unremarkable and have what can be considered “typical” values for the $\log(M_*) \sim 10.7$, and they also do not appear to be strong SBs ($\Delta\text{MS} = 3.8$ and 2.2, respectively, for 10041706 and 10100707). Furthermore, the cutouts presented in Figure 16 indicate that these sources do not appear to be blended; therefore, the only unusual characteristic that they possess seems to be an elevated M_{gas} .

A possible explanation for the very high M_{dust} and subsequently M_{gas} estimates for these galaxies, other than an extremely low δ_{GDR} , could be an optically thick FIR emission. In this scenario, the attenuation of the emission in the Wien part of the spectrum makes the galaxy appear cold, leading to an overestimate of its true M_{dust} (e.g., Jin et al. 2019; Cortzen et al. 2020). Since the DL07 models assume that the galaxy is optically thin at $\lambda_{\text{rest}} > 1 \mu\text{m}$, to test this scenario we employed MBB models of general opacity, leaving the effective wavelength (λ_{eff}) at which $\tau = 1$ as a free parameter (see, e.g., Casey et al. 2012 for the functional form). We fixed the R-J slope to $\beta = 1.8$ and only fit the available photometry of each source at $\lambda_{\text{rest}} > 40 \mu\text{m}$. Due to the large number of free parameters in this model, we further limit our sample to sources with five or more IR detections. Out of the 41 “gas giants,” we are thus able to constrain λ_{eff} for only 19. The distribution of the inferred λ_{eff} values is presented in Figure 17.

We find that the vast majority of these objects have $\lambda_{\text{eff}} > 100 \mu\text{m}$, which implies that these galaxies could be optically thick in the FIR. The unusually high f_{dust} and f_{gas} can therefore be incorrect simply as a result of the optical depth effects. Indeed, a comparison between the inferred M_{dust} estimates for an optically thin and optically thick case yields an average ratio of $\sim \times 1.8$ for our sample. However, while this correction would reduce the average f_{gas} of the “gas giants” from $\langle \log(f_{\text{gas}}) \rangle = 0.72$ to $\langle \log(f_{\text{gas}}) \rangle = 0.47$, this is still substantially larger with respect to the average population of

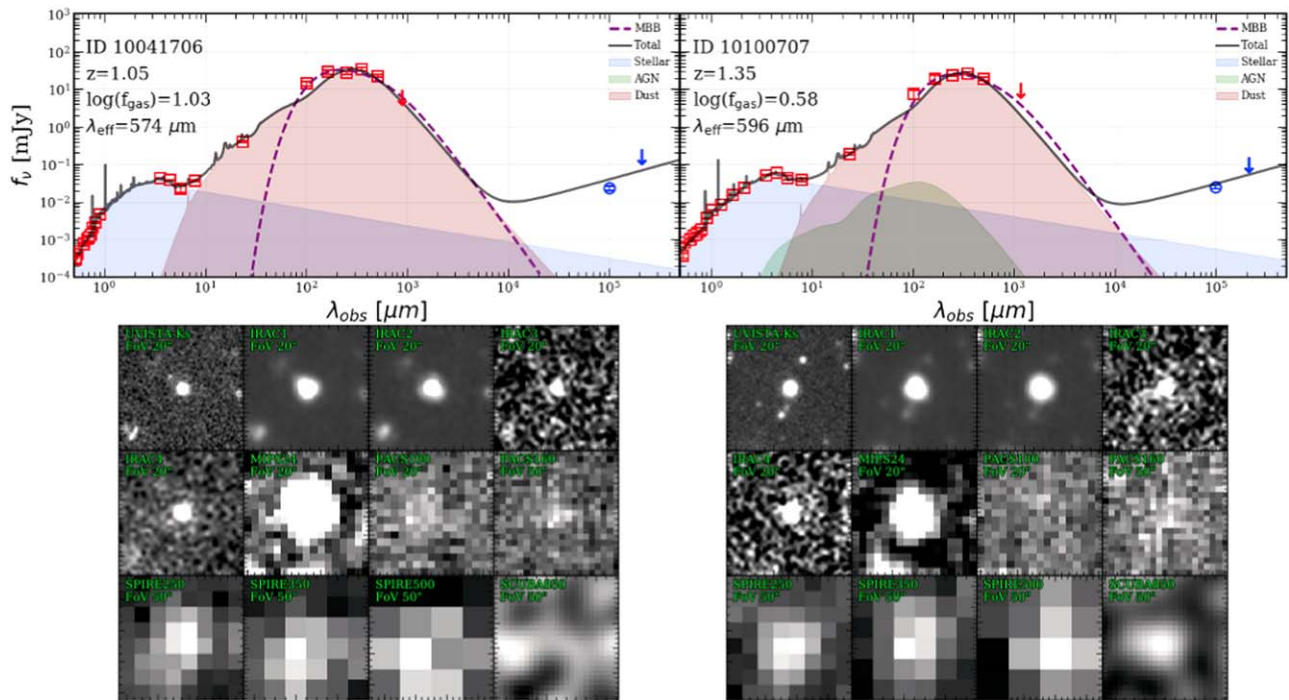


Figure 16. Top: photometry and best-fit SEDs for two “gas giants” ($\log(f_{\text{gas}}) > 0.5$) at $z_{\text{spec}} = 1.05$ and $z_{\text{spec}} = 1.35$. Color-coding and symbols are the same as in Figure 3, with the addition of a dashed purple line that shows the best-fit optically thick MBB. The λ_{eff} (in rest frame) at which the SED becomes optically thick ($\tau = 1$) is displayed in the panels. Bottom: NIR–FIR cutouts of these objects. The cutout sizes range from 20” in the NIR–MIR range to 50” in FIR.

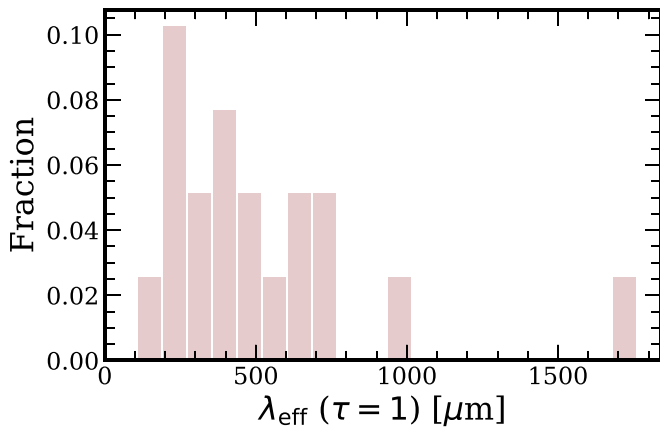


Figure 17. Distribution of λ_{eff} , below which the emission of the “gas giants” in our sample becomes optically thick ($\tau = 1$), as inferred by MBB models of general opacity.

SFGs. Finally, the real f_{gas} could in fact be lower if the M_* of the sources is underestimated, a scenario that is indeed in line with a dusty, optically thick ISM.

To understand whether these objects do indeed host unusually high gas mass reservoirs and shed light on their nature, additional observations, with either ALMA or NOEMA, of M_{gas} tracers (e.g., CO and CI) are necessary.

9. Summary

In this work we present an in-depth analysis of the evolution of the FIR properties of SFGs by studying a large sample of sources drawn from the publicly available infrared catalogs in the GOODS-N and COSMOS fields (Jin et al. 2018; Liu et al. 2018). Both catalogs are constructed based on a novel

“super-deblending” technique that allows prior-based photometry in the highly confused Herschel and SCUBA +AzTEC maps.

In the process, we developed a new panchromatic SED fitting algorithm—Stardust—to fit a linear combination of stellar, AGN, and infrared (star-forming) templates, in an attempt to perform a coherent, systematic, and homogeneous analysis in the two fields. Our fitting tool has two key advantages. First, the best-fit model is a set of coefficients rather than a single template; thus, it does not rely on iterating through thousands of possible template combinations, speeding up the fitting process by a factor of ~ 10 compared to other multiwavelength fitting available codes. Second, the fitting process does not impose energy balance between absorption in the UV/optical and emission in the IR, treating the stellar and the dust emission components independently. As such, it is very relevant for sources where the stellar emission and dust emission are not cospatial. The code itself is also highly modular, allows for user input templates, and is publicly available.

A first product of this new software is a multiparameter catalog that contains the FIR properties of ~ 5000 IR-bright galaxies in GOODS-N and COSMOS. The extracted parameters, their uncertainties, and the matched photometry from the original “super-deblended” catalogs are released and are also publicly available.²³ The list of output best-fit parameters and the structure of the released catalog can be found in Appendix A.

We subsequently used the extracted parameters to explore the evolution of the FIR properties of SFGs and recover scaling relations, aided by a careful set of simulations that quantify the underlying selection effects and biases of our sample in terms

²³ Tables containing the DMFs can be accessed at https://github.com/VasilyKokorev/sdc_ir_properties.

of limiting M_{dust} , L_{IR} , and $\langle U \rangle$. In particular, we parameterized the f_{dust} of galaxies as a function of their cosmic age, M_* , and ΔMS . The median f_{dust} is found to increase by a factor of $\times 10$ from $z = 0$ to $z = 2$ with a mild, if any, evolution at higher z . Through the metallicity-dependent δ_{GDR} technique, we also derive the evolution of f_{gas} and find it to be consistent with previous observational studies, as well as with theoretical predictions.

Furthermore, we constructed the DMF up to $z = 1$ by converting the SMF of SFGs to a DMF, through the evolution of f_{dust} and its scatter, as parameterized in our study. A comparison of the derived DMFs to the theoretical predictions of the HAGN and TNG100 simulations in the $0 < z < 0.5$ range reveals an excellent agreement down to a limiting $M_{\text{dust}} \sim 5 \times 10^7 M_{\odot}$, where, due to poor statistics, we cannot adequately constrain the $M_{\text{dust}}-M_*$ relation.

Finally, we identified a population of SFGs with extreme $\log(f_{\text{gas}}) > 0.5$, which we coin as “gas giants.” The f_{gas} excess of these galaxies compared to the average SFG population persists even when opacity effects in the FIR emission are taken into account. Follow-up observations targeting alternative M_{gas} tracers are necessary to confirm the extreme nature of these systems.

Some further remarks that we would like to emphasize:

1. The effect of the photo- z uncertainty in the derivation of M_{dust} (and L_{IR}) is not negligible and should be accounted for. We find that a photo- z uncertainty of $\Delta z / (1 + z_{\text{spec}}) \sim 0.02$, characteristic of fields like GOODS-N and COSMOS, introduces an extra 20% of scatter in the derivation of M_{dust} and L_{IR} .
2. As already discussed in the literature, the uncertainty in the derivation of M_{dust} increases substantially in the absence of a data point in the R-J tail ($\lambda_{\text{rest}} > 150 \mu\text{m}$). However, the presence of three data points in the mid-IR (MIR) to FIR could securely constrain M_{dust} within a factor of ~ 0.3 dex, even if the last available data point is at $\lambda_{\text{rest}} \approx 150 \mu\text{m}$.
3. When using the $M_{\text{dust}}-M_*-z$ scaling relations to convert SMF to DMF (or similarly to gas mass functions), the scatter of the relations used for the transformation should be taken into account for a proper comparison to the data. Similarly, any attempt to derive scaling relations between two (or more) parameters through the comparison of mass (or luminosity) functions inferred through the modeling of the observed number densities should entail a proper consideration of the scatter of the parameters in question.
4. Both the warm M_{dust} and the warm IR emission arising from the PDRs are increasing with respect to the cold M_{dust} and cold dust emission as we move above the MS, indicative of more compact/active star-forming activity. Subsequently, the clear and relatively tight trend of decreasing $M_{\text{dust}}^{\text{cold}}$ (for fixed L_{IR}) with ΔMS is less pronounced for $M_{\text{dust}}^{\text{warm}}$. This enforces the overall picture where SBs are characterized by higher star formation efficiencies and with a larger fraction of their M_{dust} being exposed to more intense radiation fields.

We thank Yohan Dubois and Clotilde Laigle for providing us with HAGN data and their input toward the discussion of simulations, Jenifer Millard for providing us with the DMF data, and Benjamin Magnelli for the help in understanding the dust mass density evolution. We also would like to thank the

anonymous referee for a number of constructive suggestions. The Cosmic Dawn Center is funded by the Danish National Research Foundation under grant No. 140. G.E.M. and F.V. acknowledge the Villum Fonden research grant 13160 “Gas to stars, stars to dust: tracing star formation across cosmic time.” F.V. acknowledges support from the Carlsberg Foundation research grant CF18-0388 “Galaxies: Rise And Death.” I.D. acknowledges support from the European Union’s Horizon 2020 research and innovation program under the Marie Skłodowska-Curie grant agreement No. 896225. S.T., G.B., and J.W. acknowledge support from the European Research Council (ERC) Consolidator Grant funding scheme (project ConTExt, grant No. 648179). S.J. acknowledges financial support from the Spanish Ministry of Science, Innovation and Universities (MICIU) under AYA2017-84061-P, co-financed by FEDER (European Regional Development Funds). D.L. acknowledges funding from the European Research Council (ERC) under the European Union’s Horizon 2020 research and innovation program (grant agreement No. 694343).

Appendix A SED Fitting

A.1. Draine & Li (2007) Templates

In our fitting routine we utilize the dust models of Draine & Li (2007), with the updated opacity from Draine et al. (2014). These models aim for a robust and physically motivated approach to SED fitting in both MIR and FIR, as well as allow us to calculate the amount of luminous dust.

The description of the dust locked in the ISM is one of a mixture of carbonaceous and amorphous silicate grains, with their sizes and distributions following the extinction law in the Milky Way, the Large Magellanic Cloud (LMC), and the bar region of the Small Magellanic Cloud (SMC). The carbonaceous grains behave similarly to the PAH molecules, with their properties given by the PAH index q_{PAH} , which is defined as a fraction of dust mass locked into the PAH grains.

The models provide a bimodal description of the environments containing the interstellar dust: the diffuse ISM and the PDRs. The bulk of the dust mass is thought to be located in the cold and diffuse part of the ISM, which is being heated by a radiation field of a constant intensity U_{min} . A smaller proportion of the mass budget described by the γ index is exposed to a gradient of radiation intensities ranging from U_{min} to U_{max} and is supposedly located in the warmer PDRs. Although these warm regions normally contain only a small fraction of the total dust mass, they can make a substantial contribution to the luminosity in the MIR SEDs. As described by DL07, the infinitesimal proportion of dM_{dust} exposed to radiation fields between U and $U + dU$ can be modeled by a power-law distribution and, in the case of the diffuse ISM where $U_{\text{min}} = U_{\text{max}}$, by a Kronecker δ -function. This leads to the following description:

$$dM_{\text{dust}} = (1 - \gamma)\delta(U - U_{\text{min}}) + \gamma M_{\text{dust}} \frac{\alpha - 1}{U_{\text{min}}^{1-\alpha} - U_{\text{max}}^{1-\alpha}}, \quad (\text{A1})$$

with $U_{\text{min}} \leq U_{\text{max}}$ and $\alpha \neq 1$. The parameter γ is the fraction of dust mass locked into the high starlight intensity regions described by the power law, α gives the distribution of radiation intensities in the PDRs, and M_{dust} is the total dust mass.

The methods described in DL07 allow us to compute a distribution of temperatures for all particles: ones that are small so their size makes them susceptible to the effects of quantized heating, and the larger ones where the steady-state temperatures dictated by the stellar radiation and radiative cooling equilibrium take hold. One can compute an averaged IR emission for a given grain type by first considering their temperature distribution and cross sections and then summing everything up to obtain the specific mass-weighted power that is being radiated by the dust exposed to starlight of intensity U . By integrating these numerical recipes from U_{\min} to U_{\max} , one can obtain the power per unit frequency per unit mass $p_\nu(q_{\text{PAH}}, U_{\min}, U_{\max}, \alpha)$.

In line with DL07, one can then model the galaxy SED as a linear combination of the diffuse ISM and the PDRs. This can be written as follows:

$$j_\nu = (1 - \gamma)j_\nu[U_{\min}, U_{\max}] + j_\nu[U_{\min}, U_{\max}, \alpha], \quad (\text{A2})$$

where j_ν is the emissivity per hydrogen nucleon. If one now considers a galaxy at some distance $D_L(z)$, the received flux density can be written as

$$f_\nu = \frac{M_{\text{H}}}{m_{\text{H}}} \frac{j_\nu}{D_L^2(z)}. \quad (\text{A3})$$

Since j_ν is the quantity contained in the DL07 models, the normalization extracted from the fitting represents the total number of hydrogen nucleons and can be then converted to the luminous dust mass.

The total luminosity contained in both dust components can be written as

$$L_{\text{dust}} = \langle U \rangle P_0 M_{\text{dust}}, \quad (\text{A4})$$

with $\langle U \rangle$ representing a mean intensity of the radiation field, given by

$$\langle U \rangle = (1 - \gamma)U_{\min} + \frac{\gamma \ln(U_{\max}/U_{\min})}{U_{\min}^{-1} - U_{\max}^{-1}}, \quad (\text{A5})$$

for $\alpha=2$ and P_0 denoting the power absorbed per unit dust mass in a radiation field of intensity $U=1$.

In principle, one could think of these models as having six effective free parameters— q_{PAH} , U_{\min} , U_{\max} , α , γ , and M_{dust} —acting as the normalization as described above. It has been shown in Draine et al. (2007) that the parameter space is insensitive to the adopted dust model (MW, LMC, and SMC) and the values of α and U_{\max} . It is thus possible to recover a wide range of properties of various SEDs by fixing these to $\alpha=2$ and $U_{\max}=10^6$. The values of U_{\min} below 0.7 correspond to temperatures below 15 K, and while it is expected to find very few systems that exhibit this behavior, we have decided not to limit the range of U_{\min} and allow it to vary between 0.1 and 50, to capture even the most extreme cases. It has been shown that, at least in the case of local galaxies in the Spitzer Nearby Galaxy Survey (SINGS), the U_{\min} can be limited between $0.7 \leq U_{\min} \leq 25$, and an MW-like dust model can be adopted to limit q_{PAH} between 0.004 and 0.046. Incorporating the use of the optimized set of parameters, which has been done in similar studies (e.g., Magdis et al. 2012a; Magnelli et al. 2012; Santini et al. 2014), might have a positive effect on computational speeds; however, we need to consider that this reduced parameter space has only been robustly verified for nearby solar-like metallicity populations of galaxies

and might otherwise risk underestimating (overestimating) the dust masses for extremely cold (warm) systems.

We can thus extract the following physical parameters from the fit: γ , q_{PAH} , U_{\min} . The dust mass is simply computed from the normalization, while the L_{IR} is L_ν integrated over the 8–1000 μm range. As an additional parameter, we can obtain $\langle U \rangle$ by utilizing Equation (A5), or alternatively, as prescribed by Magdis et al. (2012a), we can use Equation (A4), where we set $L_{\text{dust}} = L_{\text{IR}}$ and $P_0 \approx 125$.

A.2. Removing AGN Contamination

AGNs can have a significant impact on the ISM of galaxies that host them. They possess an ability to halt star formation by heating up the gas and dust or completely quenching the galaxy by stripping away its fuel. Under the common assumption (Antonucci 1993; Urry & Padovani 1995; Tristram et al. 2007), AGNs are surrounded by dusty tori, which, similarly to the ISM dust, can absorb the UV/optical light from the AGN and reradiate it at redder wavelengths, normally peaking in the MIR regime at 20–50 μm . It has also been shown that for select extreme cases (Mullaney et al. 2011) the AGN emission dominates the SED of a galaxy even at 60 μm , which presents a new challenge when calculating an infrared luminosity of a source. Infrared-derived SFR estimates rely on a robust understanding of the L_{IR} . Therefore, it is imperative to separate the energy contributions from hot dust in the ISM and a possible AGN.

In order to account for the effects of the IR contamination by AGNs when calculating L_{IR} , as well as to identify all the possible systems that might contain an active nucleus in our sample, we have decided to adopt a set of AGN templates from Mullaney et al. (2011, hereafter M11). These templates have been empirically derived by assuming an MBB function and fitting it to a set of Swift-BAT AGNs and IRAS spectra. The obtained models describe intrinsic AGN emissions in the range spanning from MIR to FIR (6–100 μm). In this case, a typical AGN SED could be thought of as a broken power law at $\leq 40 \mu\text{m}$, which rapidly vanishes when moving above 40 μm . The average intrinsic AGN emission can be described as follows:

$$F_\nu = \begin{cases} \lambda^{1.8} & \text{at } 6 \mu\text{m} < \lambda < 19 \mu\text{m} \\ \lambda^\alpha & \text{at } 19 \mu\text{m} < \lambda < 40 \mu\text{m}, \\ \nu^{1.5} F_\nu^{\text{BB}} & \text{at } \lambda > 40 \mu\text{m} \end{cases}, \quad (\text{A6})$$

where F_ν^{BB} is the MBB function and α is the spectral index. In our procedure we utilize the high- and low-luminosity templates, with $\alpha=0.0$ and 0.4, respectively. In addition to that, we allow for a linear combination between the two, with varying coefficients, thus expanding the existing template space.

A.3. Stellar Emission Component

The contribution of stellar emission in the observed NIR bands, such as Spitzer IRAC 1-4, can be quite significant, especially when we move to higher z . Therefore, if no libraries representing the luminosity from dust-attenuated stellar light are available, one might either underestimate the slope of the AGN or overestimate its normalization. This can lead to erroneously assigning more luminosity to the AGN component in the MIR and therefore underestimating the L_{IR} .

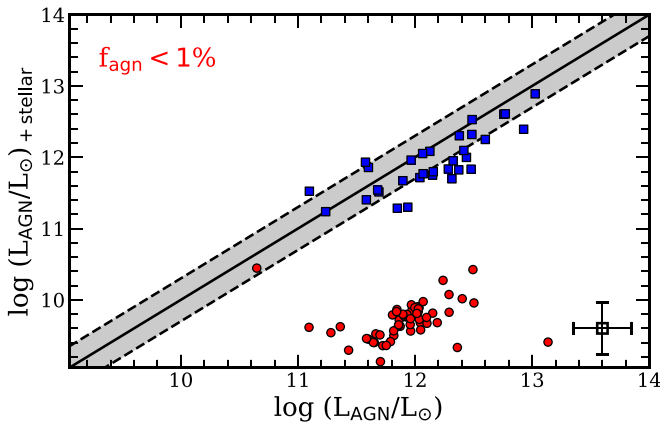


Figure 18. A comparison between fits that incorporate the stellar component and those that do not for $z > 2$ galaxies. Blue squares and red circles represent objects that were assigned $f_{\text{AGN}} > 0.01$ and $f_{\text{AGN}} < 0.01$, respectively, by the means of our three-component fit. The median uncertainty for both quantities is in the lower right corner. The black solid line represents the 1:1 relation, and the gray regions cover the 0.3 dex range.

To avoid this, we additionally incorporate a library of stellar emission models, which are an updated version of the templates described by Brammer et al. (2008, hereafter GB08). These are based on the SPS models (Conroy et al. 2009), which were optimized for deep optical–NIR broadband surveys. The models form a basis set of a larger library and were derived by using the “nonnegative matrix factorization” algorithm that was described in Blanton & Roweis (2007). The method attempts to reproduce the full library of templates, by finding a nonnegative linear combination of a smaller number of models. These can be considered as the “principal component” blueprint of the larger catalog. In total, there are 12 optical SEDs, which include both dust-attenuated and nonattenuated starlight. We have incorporated these models into our fitting routine, and if the UV–optical photometry is available, this allows us to extract properties such as M_* , SFR, $E(B-V)$, and SFH. If no UV–optical data are available, the addition of these templates is still useful, as they can account for the excess flux in the rest-frame NIR bands, in conjunction with AGN and IR templates.

To test how our fits behave without the stellar component, we have isolated ~ 100 objects with $z > 2$, so that our bluest available band traces $\lambda_{\text{rest}} \sim 1 \mu\text{m}$, where the contribution from stellar emission becomes nonnegligible. We then exclude GB08 templates and refit our objects. This results in two outcomes that can be seen in Figure 18. We find that, by removing the additional component, we tend to either overestimate the AGN contribution (blue squares), with the median being ~ 1.5 , or alternatively erroneously assign a galaxy to contain an AGN (red points).

A.4. Bringing It All Together

In order to model an SED of a galaxy and extract the physical parameters, we first transport all three components—the stellar, the dusty torus AGN, and the infrared dust emission—to a common wavelength grid spanning the range from 10^{-4} to $10^5 \mu\text{m}$. Our method relies on a linear combination of these models, thus making it imperative for them to share a common range, so that co-adding them is made possible. In certain cases where this grid falls outside the original range of the template, we extrapolate blueward and redward by using a steeply

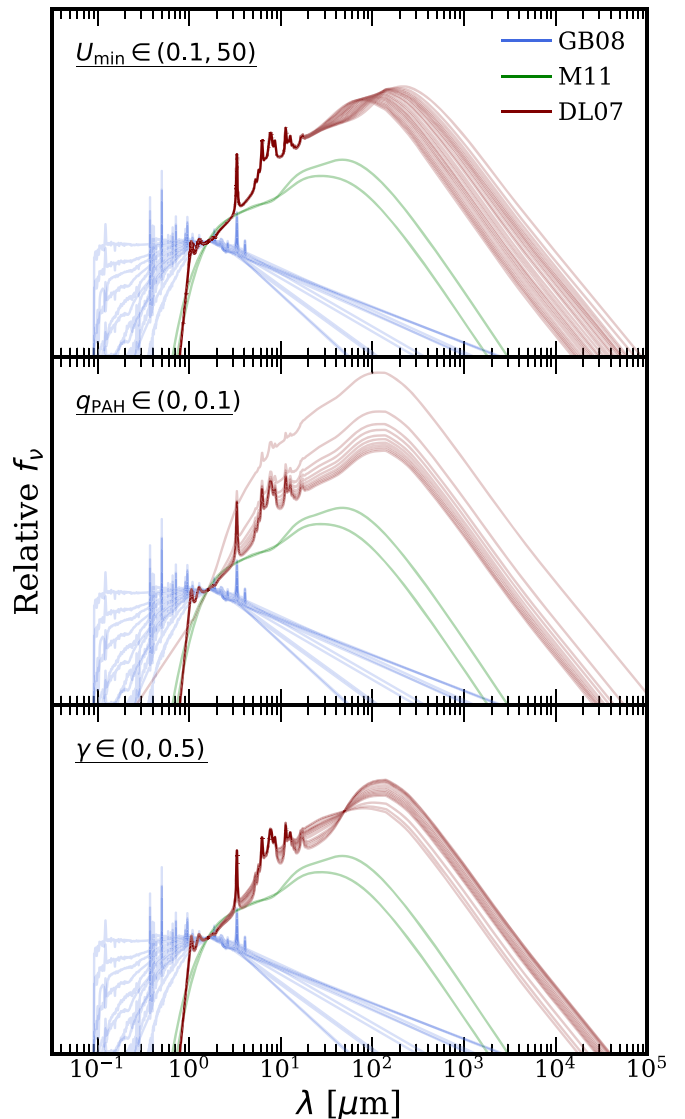


Figure 19. A compilation of all template flavors used in *Stardust*. Color-coding is blue, green, and maroon for Brammer et al. (2008) UV–optical SPS models, Mullaney et al. (2011) AGN models, and Draine et al. (2007) IR dust models, respectively. We show the variations in U_{min} , q_{PAH} , and γ separately in each panel, while other parameters are fixed. For visualization purposes all templates shown here have been normalized to the K band.

declining power law. This was done to ensure that the resultant galaxy emission is continuous without any sudden breaks, which could interfere with the fitting, where one of the templates has ran out of range. These added power laws do not introduce any additional emission, as the flux density contribution from them is orders of magnitude lower than that of the original template. We then redshift the wavelength grid on a per-galaxy basis and normalize the templates to ensure that they are not separated by tens of orders of magnitude. In Figure 19 we show all the templates used in *Stardust*, normalized to the K band, and in Table 2 we list all the relevant parameters of the models.

Subsequently, we perform a synthetic photometry on all three components separately in all observed bands where data are available. This is done by convolution of the filter transmission curves with the model SEDs. The resultant synthetic fluxes for each template and available observed band

Table 2
Template Parameters Used for `Stardust` Fit

Parameter	Value
Dust Emission: DL07 (Updated in Draine et al. (2014))	
U_{\min}	[0.1, 0.2, 0.3, 0.4, 0.5, 0.6, 0.7, 0.8, 1.0, 1.7, 2.0, 3.0, 4.0, 5.0, 7.0, 8.0, 10.0, 12.0, 15.0, 20.0, 25.0], 26 values
q_{PAH}	[0; 0.1], 11 values in steps of 0.1
γ	[0, 0.001, 0.0025, 0.005, 0.0075] +[0.01; 0.1], 9 values in steps of 0.01 +[0.2, 0.35, 0.5], 17 values in total
Optical Emission: Brammer et al. (2008) ^a	
A_V (Calzetti et al. 2000)	[0.6, 0.12, 0.19, 0.29, 1.05, 2.68, 0.11, 0.36, 0.98, 1.54, 1.97, 2.96]
M/L_V	[0.38, 0.76, 1.68, 4.01, 6.45, 44.48, 0.12, 0.21, 0.33, 0.64, 1.57, 4.00]
$\log_{10}(\text{sSFR})$	[-10.75, -11.37, -11.90, -12.53, -12.05, -12.47, -8.37, -8.60, -8.50, -8.57, -8.93, -8.90]

Note.

^a Please refer to [Brammer et al. \(2008\)](#) for a more detailed description of the creation and selection of these basis-set templates. See [Blanton & Roweis \(2007\)](#) for a methodology regarding the SFH.

are then all combined into a two-dimensional matrix and passed onto the nonnegative least-squares (nnls) algorithm in the Python `scipy.optimize.nnls` package, which finds the best solution vector for that object. The nnls is a simple minimization algorithm that in our case takes the form of

$$\min \|A_{b,t}x^t - y^b\|_2 \quad \text{where } x \geq 0, \quad (\text{A7})$$

where A is the uncertainty-weighted template matrix, y is the S/N for each band, x is the solution vector, and $\|\cdot\|_2$ signifies the Euclidean norm. Instead of finding the best-fitting template, the algorithm computes the best-fit coefficients x , with $x \geq 0$. The number of simultaneously fit templates is user defined. For our purposes we chose to fit all 12 [GB08](#) and 2 [M11](#) templates at the same time, each time combining them with a single [DL07](#) template, iterating through all the possible combinations, and then finding the best fit. Following Equation (A7), this is done by building the matrix A , for each band b and each template t , where the first 14 templates in the matrix remain fixed, while the last element is being continuously replaced with a new [DL07](#) model and looped over. In the end we obtain 4862 possible best-fit vectors— x^t , one per each [DL07](#) model. The final result is then extracted from the χ^2 distribution of all best-fit solutions. The advantage of this method is in avoiding progressively looping over all possible template combinations to find the best solution, and instead only choosing to loop through [DL07](#) templates. This approach significantly reduces the amount of required computational resources. The resultant solution vector encodes the individual contributions from each template to the total emitted flux in each band. These are then

Table 3
Structure of the Best-fit Catalog^a

Column Name	Units	Description
Catalog	...	Catalog identifier code
ID	...	ID of the object from the parent catalog
R.A.	deg	R.A. coordinate, as given in the parent catalog
Decl.	deg	Decl. coordinate, as given in the parent catalog
Area	...	Same as <code>goodArea</code> flag in the parent catalogs
z	...	Redshift used for fitting
ztype	...	Redshift type, 1 for spectroscopic, 0 for photometric, and 2 for z_{phot} from EAZY
LIR_total	L_{\odot}	Total FIR luminosity, obtained as the sum between AGN and DL07 components
eLIR_total	L_{\odot}	Uncertainty on the total FIR luminosity
Lagn_total	L_{\odot}	AGN luminosity
eLagn_total	L_{\odot}	Uncertainty on the AGN luminosity
Lir_draine	L_{\odot}	Luminosity given by the DL07 template
eLir_draine	L_{\odot}	Uncertainty on the luminosity given by the DL07 template
MD	M_{\odot}	Dust mass as predicted by the best-fit DL07 template
eMD	M_{\odot}	Uncertainty on the dust mass
deltaGDR	...	Gas-to-dust ratio
MG	M_{\odot}	Gas mass computed from δ_{GDR} and M_{dust}
eMG	M_{\odot}	Uncertainty on gas mass
Mstar	M_{\odot}	Stellar mass, equal to the one in the original catalog
lastdet	μm	Last band that has an S/N > 3 detection (λ_{last}); given in rest frame
chi2	...	The χ^2 of the best-fit coefficients
f_agn	...	AGN fraction, given as $L_{\text{AGN}}/L_{\text{IR,total}}$
efagn	...	Uncertainty on the AGN fraction
fgas	...	Gas fraction computed as $M_{\text{gas}}/M_{\text{dust}}$
fgas_FMR	...	Gas fraction computed assuming $\delta_{\text{GDR}} = 100$
Umin	...	Best-fit U_{\min}
gamma	...	Best-fit γ
qpah	...	Index of the best-fit q_{PAH} value
U	...	Average radiation field intensity $\langle U \rangle$
sU	...	Uncertainty on $\langle U \rangle$
deltaMS	...	SFR/SFR _{MS} , where SFR = $L_{\text{IR,draine}} \times 10^{-10}$ and SFR _{MS} is given by Schreiber et al. (2015)
e_deltaMS	...	Uncertainty on ΔMS

Notes.

^a `Stardust` also returns M_* , A_V , and UV–optical SFR; these are not included in the release version of the catalog but are available upon request.

^b We have used the 7970d55 (28/06/21) version of `Stardust` to produce these catalogs.

(This table is available in its entirety in machine-readable form.)

added together to return the best-fit solution. This three-component split allows us to predict exactly how much each component contributes to the source’s L_{IR} , thus allowing us to differentiate between the AGN and the warm ISM dust emissions. In addition to that, the normalization of [DL07](#) templates leads us directly to the number of hydrogen nucleons, linking it to dust mass via Equation (A4). The radio data points are not being considered by our fitting routine; however, we add a power-law radio slope with a spectral index of -0.75 , as described by the FIR–radio correlation in [Delvecchio et al. \(2021\)](#), mainly for visualization purposes, but also to detect the existence of the AGN radio excess.

A.5. Calculating the IR Properties

To derive luminosity estimates, we integrate the three-component summed SED in the 8–1000 μm . This gives us the $L_{\text{IR,tot}}$ that contains within itself the energy emitted by the ISM dust and AGN torus, if present. The contribution of stellar emission at $\lambda_{\text{rest}} > 8 \mu\text{m}$ is negligible; therefore, we do not go through an additional step of subtracting those models. We then integrate the best-fit template with just the AGN contribution in it, to obtain the L_{AGN} and $L_{\text{IR}} = L_{\text{IR,tot}} - L_{\text{AGN}}$. We also compute the $f_{\text{AGN}} = L_{\text{AGN}}/L_{\text{IR,tot}}$ to estimate how strongly the infrared SED of a galaxy is contaminated by AGN activity. In addition to that, it allows us to separate our sample into objects that have an active nucleus and those that do not. The conditions of the ISM in these different environments may vary quite significantly and would affect the extracted scaling relations if not treated correctly.

The normalization of the DL07 models returns the number of hydrogen nucleons as one of its free parameters, from which we can obtain the fiducial M_{H} . We then compute M_{dust} by converting this quantity assuming a fixed gas-to-dust ratio of $\delta_{\text{GDR}} = 100$, as prescribed in DL07. It is important to note that this ratio is encoded into the models and does not represent an actual physically meaningful conversion factor. We also compute a T_{dust} proxy in the form of the average radiation field intensity $\langle U \rangle$, from Equation (A4), by assuming a $P_0 = 125$. We note, however, that this quantity represents the luminosity-weighted dust temperature and has little to no bearing on the temperature of the cold dust or gas (see, e.g., Scoville et al. 2016, 2017). The structure of the final output catalog is presented in Table 3.

Appendix B Stellar Mass Comparison

To test the robustness of Stardust-derived M_* estimates, we start by first comparing them to the M_* as given by the original catalog. The SDC2 takes its M_* directly from the COSMOS 2015 catalog (Laigle et al. 2016), which uses SED fitting code LePhare (Arnouts et al. 1999; Ilbert et al. 2006) to constrain the photometric redshift, M_* , and a host of other parameters. Similarly to our approach, LePhare relies on Bruzual & Charlot (2003) simple stellar population (SSP) libraries to fit galaxy SEDs. We begin our fitting procedure by carefully correcting all the COSMOS 2015 aperture fluxes to total fluxes, as well as correcting for the MW extinction, as prescribed in Laigle et al. (2016). We then cross-match these sources to SDC2, by using the K band, and fit the entirety of the 36 available bands with our code. As a sanity check, we additionally run the same photometric catalog through EAZY, albeit stopping at IRAC 2.

We present this comparison in Figure 20. The M_* given by the parent catalog and the ones derived by Stardust-derived M_* agree very well, with Stardust on average under-predicting the M_* by ~ 0.01 dex. We attribute a considerable 0.31 dex scatter to the fact that in their LePhare fit Laigle et al. have used an iterative procedure, which involved correcting the observed fluxes in order to match the colors of the model library.

More reassuringly, we find a good correlation when comparing our M_* to EAZY, with a median offset of -0.03 dex and a minor 0.15 dex scatter being most likely induced by the fact that with Stardust we fit the entire available spectrum from UV to FIR, as opposed to just UV–optical, with EAZY.

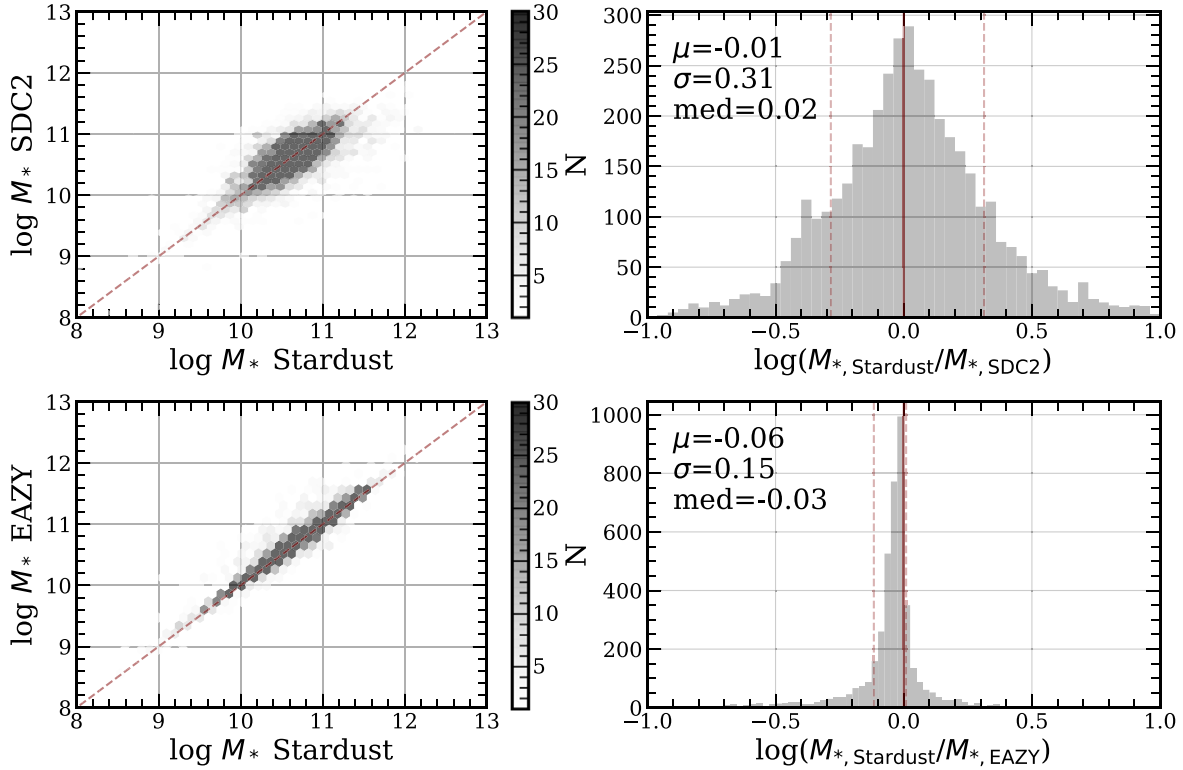


Figure 20. Comparison of the Stardust-derived M_* vs. SDC2 (top) and EAZY (bottom). The dashed maroon line represents a 1:1 relation. The solid and dashed maroon lines represent a 1:1 relation and the 68% confidence interval, respectively.

Appendix C Comparison with CIGALE

In order to better understand how our independent linear combination approach compares to the energy balance method, we have fit our sources with CIGALE. For this we have utilized a set of SSP models from Bruzual & Charlot (2003) for the nonobscured stellar light; the revised version of the Draine & Li (2007) templates for the obscured stellar light, reprocessed by dust; and Fritz et al. (2006) for the AGN contribution. The attenuation law that we considered was described in Calzetti et al. (2000). For the SSP templates, we have assumed a single delayed SFH. These CIGALE fits should be treated as a “basic” first-pass approach, due to the computational limitations necessitating a constrained range for the template parameters. Ideally, such an analysis would require a flexible SFH, in order to obtain better SFR, as well as a wider range of parameters, for both the DL07 and Fritz et al. templates.

We show the comparison between the two methods in Figure 21. There is a very good agreement between the M_{dust} derived with our code and CIGALE, with the difference having a mean of 0.09 dex and median of 0.02 dex. The derived values of L_{IR} are, however, in tension, with a mean of 0.20 dex and median of 0.11 dex. We attribute the significant outliers ($>1\sigma$) to cases where the energy balance method in CIGALE has

failed to account for the extra FIR flux. We also compare the Stardust- and CIGALE-computed M_* and find that the two agree within 0.1 dex, albeit with a significant 0.3 dex scatter. As we have already discussed in Section 3, in certain environments the stellar emission and the dust emission could be spatially disconnected; thus, the energy balance might not be the best physically motivated option. In addition, when dealing with extreme sources, the Calzetti et al. attenuation law might not allow the energy balance approach to account for all IR flux (see, e.g., Buat et al. 2019). The above, however, are not the only explanations, as the identification/matching problems and IR flux extractions could also play a part in creating this tension between our results and CIGALE (see, e.g., Małek et al. 2018).

When directly comparing computation times, it is important to note that CIGALE fits sources within redshift blocks, where it precompiles a set of models first and then estimates the best-fit parameters, while Stardust fits sources sequentially. As such, despite both methods being parallelized, it is difficult to achieve a fair comparison between the two. Within a single redshift block, which numbers 288 objects, CIGALE has computed 50×10^6 models and found the best fit in about 2.5 hr. Due to how the linear combination is performed within Stardust, defining an exact number of models attempted is not possible. However, considering that the 12 optical

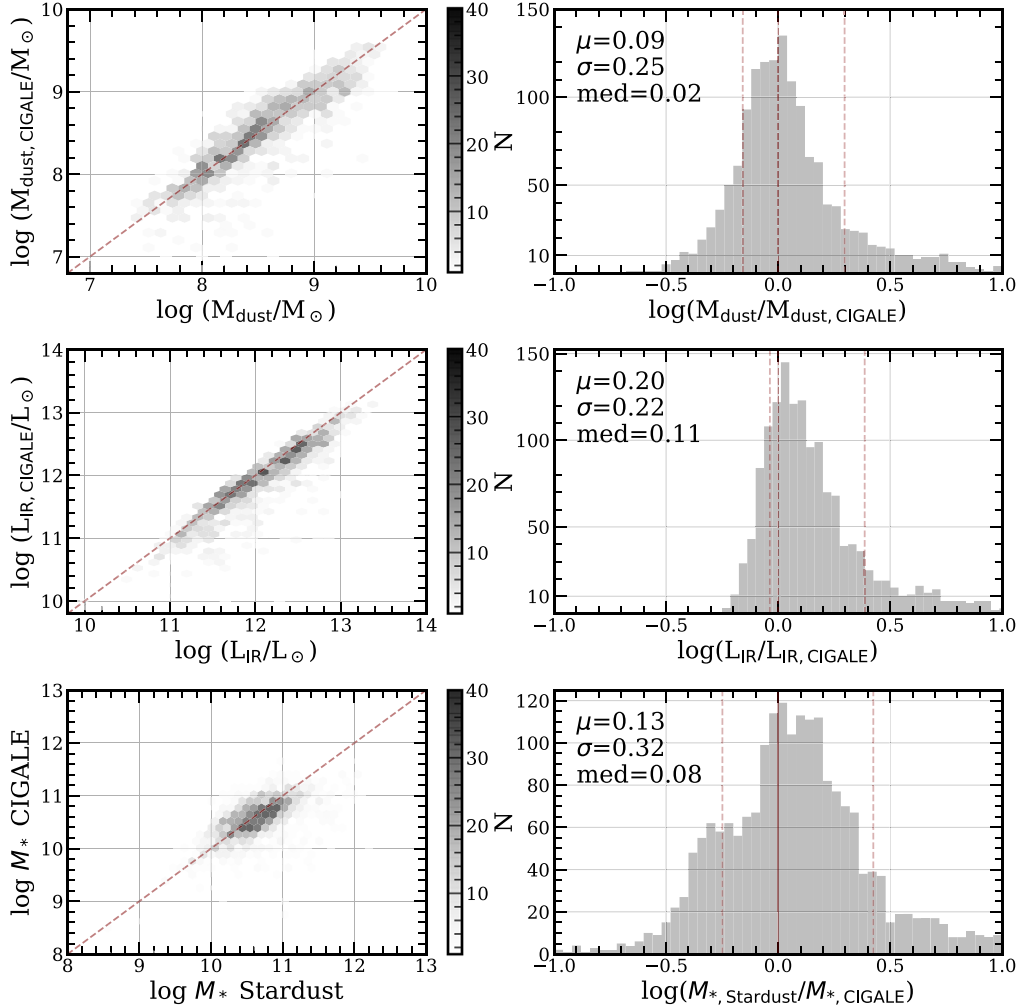


Figure 21. Comparison of the derived M_{dust} (top) and L_{IR} (bottom) between Stardust and CIGALE. The solid and dashed maroon lines represent a 1:1 relation and the 68% confidence interval, respectively.

templates have been constructed as a basis set of ~ 3000 models described in Brammer et al. (2008) and combining that with two AGN templates and ~ 4800 DL07 models results in roughly 30×10^6 total effective model combinations. Our code then takes 14 minutes in total to fit the same 288 objects, which is approximately 11 times faster than CIGALE, for the same number of CPU cores.

ORCID iDs

Vasily I. Kokorev  <https://orcid.org/0000-0002-5588-9156>
 Georgios E. Magdis  <https://orcid.org/0000-0002-4872-2294>
 Iary Davidzon  <https://orcid.org/0000-0002-2951-7519>
 Gabriel Brammer  <https://orcid.org/0000-0003-2680-005X>
 Francesco Valentino  <https://orcid.org/0000-0001-6477-4011>
 Emanuele Daddi  <https://orcid.org/0000-0002-3331-9590>
 Daizhong Liu  <https://orcid.org/0000-0001-9773-7479>
 Shuowen Jin  <https://orcid.org/0000-0002-8412-7951>
 Isabella Cortzen  <https://orcid.org/0000-0001-9197-7623>
 Ivan Delvecchio  <https://orcid.org/0000-0001-8706-2252>
 Clara Giménez-Arteaga  <https://orcid.org/0000-0001-9419-9505>
 Carlos Gómez-Guijarro  <https://orcid.org/0000-0002-4085-9165>
 Mark Sargent  <https://orcid.org/0000-0003-1033-9684>
 Sune Toft  <https://orcid.org/0000-0003-3631-7176>
 John R. Weaver  <https://orcid.org/0000-0003-1614-196X>

References

- Aniano, G., Draine, B. T., Hunt, L. K., et al. 2020, *ApJ*, 889, 150
 Antonucci, R. 1993, *ARA&A*, 31, 473
 Aoyama, S., Hirashita, H., Lim, C.-F., et al. 2019, *MNRAS*, 484, 1852
 Arnouts, S., Cristiani, S., Moscardini, L., et al. 1999, *MNRAS*, 310, 540
 Avni, Y. 1976, *ApJ*, 210, 642
 Battisti, A. J., da Cunha, E., Grasha, K., et al. 2019, *ApJ*, 882, 61
 Beeston, R. A., Wright, A. H., Maddox, S., et al. 2018, *MNRAS*, 479, 1077
 Bendo, G. J., Galliano, F., & Madden, S. C. 2012, *MNRAS*, 423, 197
 Berta, S., Lutz, D., Genzel, R., Förster-Schreiber, N. M., & Tacconi, L. J. 2016, *A&A*, 587, A73
 Berta, S., Lutz, D., Santini, P., et al. 2013, *A&A*, 551, A100
 Bertoldi, F., Carilli, C., Aravena, M., et al. 2007, *ApJS*, 172, 132
 Béthermin, M., Daddi, E., Magdis, G., et al. 2015, *A&A*, 573, A113
 Béthermin, M., Fudamoto, Y., Ginolfi, M., et al. 2020, *A&A*, 643, A2
 Blanton, M. R., & Roweis, S. 2007, *AJ*, 133, 734
 Boquien, M., Burgarella, D., Roehly, Y., et al. 2019, *A&A*, 622, A103
 Boquien, M., Calzetti, D., Combes, F., et al. 2011, *AJ*, 142, 111
 Brammer, G. B., van Dokkum, P. G., & Coppi, P. 2008, *ApJ*, 686, 1503
 Brinchmann, J., Charlot, S., White, S. D. M., et al. 2004, *MNRAS*, 351, 1151
 Bruzual, G., & Charlot, S. 2003, *MNRAS*, 344, 1000
 Buat, V., Ciesla, L., Boquien, M., Malek, K., & Burgarella, D. *A&A*, 632, A79
 Burgarella, D., Buat, V., & Iglesias-Páramo, J. 2005, *MNRAS*, 360, 1413
 Calistro Rivera, G., Hodge, J. A., Smail, I., et al. 2018, *ApJ*, 863, 56
 Calistro Rivera, G., Lusso, E., Hennawi, J., & Hogg, D. W. 2016, *ApJ*, 833, 98
 Calzetti, D., Armus, L., Bohlin, R. C., et al. 2000, *ApJ*, 533, 682
 Carilli, C. L., & Walter, F. 2013, *ARA&A*, 51, 105
 Casey, C. M., Berta, S., Béthermin, M., et al. 2012, *ApJ*, 761, 140
 Casey, C. M., Zavala, J. A., Aravena, M., et al. 2019, *ApJ*, 887, 55
 Casey, C. M., Zavala, J. A., Spilker, J., et al. 2018, *ApJ*, 862, 77
 Chabrier, G. 2003, *PASP*, 115, 763
 Chang, Y.-Y., Le Floc'h, E., Juneau, S., et al. 2017, *MNRAS*, 466, L103
 Chen, C.-C., Hodge, J. A., Smail, I., et al. 2017, *ApJ*, 846, 108
 Chen, Y.-M., Wild, V., Kauffmann, G., et al. 2009, *MNRAS*, 393, 406
 Cibinel, A., Daddi, E., Sargent, M. T., et al. 2019, *MNRAS*, 485, 5631
 Cochrane, R. K., Best, P. N., Smail, I., et al. 2021, *MNRAS*, 503, 2622
 Cochrane, R. K., Hayward, C. C., Anglés-Alcázar, D., et al. 2019, *MNRAS*, 488, 1779
 Conroy, C., Gunn, J. E., & White, M. 2009, *ApJ*, 699, 486
 Cortzen, I., Magdis, G. E., Valentino, F., et al. 2020, *A&A*, 634, L14
 Cousin, M., Buat, V., Lagache, G., & Béthermin, M. 2019, *A&A*, 627, A132
 da Cunha, E., Charlot, S., & Elbaz, D. 2008, *MNRAS*, 388, 1595
 Daddi, E., Dickinson, M., Morrison, G., et al. 2007, *ApJ*, 670, 156
 Daddi, E., Elbaz, D., Walter, F., et al. 2010, *ApJL*, 714, L118
 Dale, D. A., Aniano, G., Engelbracht, C. W., et al. 2012, *ApJ*, 745, 95
 Dale, D. A., Helou, G., Magdis, G. E., et al. 2014, *ApJ*, 784, 83
 Davé, R., Anglés-Alcázar, D., Narayanan, D., et al. 2019, *MNRAS*, 486, 2827
 Davé, R., Crain, R. A., Stevens, A. R. H., et al. 2020, *MNRAS*, 497, 146
 Davé, R., Finlator, K., & Oppenheimer, B. D. 2012, *MNRAS*, 421, 98
 Davé, R., Rafieeferantsoa, M. H., Thompson, R. J., & Hopkins, P. F. 2017, *MNRAS*, 467, 115
 Davidzon, I., Ilbert, O., Faisst, A. L., Sparre, M., & Capak, P. L. 2018, *ApJ*, 852, 107
 Davidzon, I., Ilbert, O., Laigle, C., et al. 2017, *A&A*, 605, A70
 Dekel, A., Sari, R., & Ceverino, D. 2009, *ApJ*, 703, 785
 Delvecchio, I., Daddi, E., Sargent, M. T., et al. 2021, *A&A*, 647, A123
 Dickinson, M., Giavalisco, M., & GOODS Team 2003, in Proc. of the European Southern Observatory, The Mass of Galaxies at Low and High, ed. R. Bender & A. Renzini (Berlin: Springer), 324
 Donevski, D., Lapi, A., Malek, K., et al. 2020, *A&A*, 644, A144
 Draine, B. T., Aniano, G., Krause, O., et al. 2014, *ApJ*, 780, 172
 Draine, B. T., Dale, D. A., Bendo, G., et al. 2007, *ApJ*, 663, 866
 Draine, B. T., & Li, A. 2007, *ApJ*, 657, 810
 Driver, S. P., Andrews, S. K., da Cunha, E., et al. 2018, *MNRAS*, 475, 2891
 Dubois, Y., Pichon, C., Welker, C., et al. 2014, *MNRAS*, 444, 1453
 Dunlop, J. S., McLure, R. J., Biggs, A. D., et al. 2017, *MNRAS*, 466, 861
 Dunne, L., Gomez, H. L., da Cunha, E., et al. 2011, *MNRAS*, 417, 1510
 Eales, S., Smith, M. W. L., Auld, R., et al. 2012, *ApJ*, 761, 168
 Elbaz, D., Daddi, E., Le Borgne, D., et al. 2007, *A&A*, 468, 33
 Elbaz, D., Dickinson, M., Hwang, H. S., et al. 2011, *A&A*, 533, A119
 Elbaz, D., Hwang, H. S., Magnelli, B., et al. 2010, *A&A*, 518, L29
 Elbaz, D., Leiton, R., Nagar, N., et al. 2018, *A&A*, 616, A110
 Erfanianfar, G., Popesso, P., Finoguenov, A., et al. 2016, *MNRAS*, 455, 2839
 Feltre, A., Hatziminaoglou, E., Hernán-Caballero, A., et al. 2013, *MNRAS*, 434, 2426
 Franco, M., Elbaz, D., Béthermin, M., et al. 2018, *A&A*, 620, A152
 Franco, M., Elbaz, D., Zhou, L., et al. 2020, *A&A*, 643, A30
 Fritz, J., Franceschini, A., & Hatziminaoglou, E. 2006, *MNRAS*, 366, 767
 Galamez, M., Albrecht, M., Kennicutt, R., et al. 2014, *MNRAS*, 439, 2542
 Geach, J. E., Dunlop, J. S., Halpern, M., et al. 2017, *MNRAS*, 465, 1789
 Geach, J. E., Smail, I., Moran, S. M., et al. 2011, *ApJL*, 730, L19
 Genzel, R., Tacconi, L. J., Lutz, D., et al. 2015, *ApJ*, 800, 20
 Goldsmith, P. F. 2001, *ApJ*, 557, 736
 Gómez-Guijarro, C., Toft, S., Karim, A., et al. 2018, *ApJ*, 856, 121
 Groves, B. A., Schinnerer, E., Leroy, A., et al. 2015, *ApJ*, 799, 96
 Hayward, C. C., Lanz, L., Ashby, M. L. N., et al. 2014, *MNRAS*, 445, 1598
 Hayward, C. C., Narayanan, D., Kereš, D., et al. 2013, *MNRAS*, 428, 2529
 Hodge, J. A., & da Cunha, E. 2020, *RSOS*, 7, 200556
 Hodge, J. A., Smail, I., Walter, F., et al. 2019, *ApJ*, 876, 130
 Hodge, J. A., Swinbank, A. M., Simpson, J. M., et al. 2016, *ApJ*, 833, 103
 Ilbert, O., Arnouts, S., McCracken, H. J., et al. 2006, *A&A*, 457, 841
 Imar, N., Loeb, A., Johnson, B. D., Conroy, C., & Behroozi, P. 2018, *ApJ*, 854, 36
 Jin, S., Daddi, E., Liu, D., et al. 2018, *ApJ*, 864, 56
 Jin, S., Daddi, E., Magdis, G. E., et al. 2019, *ApJ*, 887, 144
 Kaasinen, M., Walter, F., Novak, M., et al. 2020, *ApJ*, 899, 37
 Karim, A., Schinnerer, E., Martínez-Sansigre, A., et al. 2011, *ApJ*, 730, 61
 Kashino, D., Silverman, J. D., Rodighiero, G., et al. 2013, *ApJL*, 777, L8
 Kennicutt, Robert C. 1998, *J. ARA&A*, 36, 189
 Kewley, L. J., & Dopita, M. A. 2002, *ApJS*, 142, 35
 Kewley, L. J., & Ellison, S. L. 2008, *ApJ*, 681, 1183
 Kriek, M., van Dokkum, P. G., Labbé, I., et al. 2009, *ApJ*, 700, 221
 Krumholz, M. R., Klein, R. I., & McKee, C. F. 2011, *ApJ*, 740, 77
 Kurczynski, P., Gawiser, E., Acquaviva, V., et al. 2016, *ApJL*, 820, L1
 Lacey, C. G., Baugh, C. M., Frenk, C. S., et al. 2016, *MNRAS*, 462, 3854
 Lagos, C. d. P., Crain, R. A., Schaye, J., et al. 2015, *MNRAS*, 452, 3815
 Lagos, C. d. P., da Cunha, E., Robotham, A. S. G., et al. 2020, *MNRAS*, 499, 1948
 Lagos, C. d. P., Robotham, A. S. G., Trayford, J. W., et al. 2019, *MNRAS*, 489, 4196
 Laigle, C., Davidzon, I., Ilbert, O., et al. 2019, *MNRAS*, 486, 5104
 Laigle, C., McCracken, H. J., Ilbert, O., et al. 2016, *ApJS*, 224, 24
 Lee, K.-S., Ferguson, H. C., Wiklind, T., et al. 2012, *ApJ*, 752, 66
 Lee, N., Sanders, D. B., Casey, C. M., et al. 2015, *ApJ*, 801, 80
 Leja, J., Johnson, B. D., Conroy, C., & van Dokkum, P. 2018, *ApJ*, 854, 62
 Leroy, A. K., Bolatto, A., Gordon, K., et al. 2011, *ApJ*, 737, 12

- Leslie, S. K., Schinnerer, E., Liu, D., et al. 2020, *ApJ*, 899, 58
- Liang, L., Feldmann, R., Kereš, D., et al. 2019, *MNRAS*, 489, 1397
- Lilly, S. J., Carollo, C. M., Pipino, A., Renzini, A., & Peng, Y. 2013, *ApJ*, 772, 119
- Liu, D., Daddi, E., Dickinson, M., et al. 2018, *ApJ*, 853, 172
- Liu, D., Daddi, E., Schinnerer, E., et al. 2021, *ApJ*, 909, 56
- Liu, D., Lang, P., Magnelli, B., et al. 2019a, *ApJS*, 244, 40
- Liu, D., Schinnerer, E., Groves, B., et al. 2019b, *ApJ*, 887, 235
- Loveday, J., Peterson, B. A., Efstathiou, G., & Maddox, S. J. 1992, *ApJ*, 390, 338
- Lutz, D., Poglitsch, A., Altieri, B., et al. 2011, *A&A*, 532, A90
- Maddox, S. J., Valiante, E., Cigan, P., et al. 2018, *ApJS*, 236, 30
- Magdis, G. E., Daddi, E., Béthermin, M., et al. 2012a, *ApJ*, 760, 6
- Magdis, G. E., Daddi, E., Elbaz, D., et al. 2011, *ApJL*, 740, L15
- Magdis, G. E., Daddi, E., Sargent, M., et al. 2012b, *ApJL*, 758, L9
- Magdis, G. E., Elbaz, D., Daddi, E., et al. 2010, *ApJ*, 714, 1740
- Magdis, G. E., Gobat, R., Valentino, F., et al. 2021, *A&A*, 647, A33
- Magdis, G. E., Rigopoulou, D., Daddi, E., et al. 2017, *A&A*, 603, A93
- Magdis, G. E., Rigopoulou, D., Helou, G., et al. 2013, *A&A*, 558, A136
- Magnelli, B., Boogaard, L., Decarli, R., et al. 2020, *ApJ*, 892, 66
- Magnelli, B., Lutz, D., Saintonge, A., et al. 2014, *A&A*, 561, A86
- Magnelli, B., Lutz, D., Santini, P., et al. 2012, *A&A*, 539, A155
- Magnelli, B., Popesso, P., Berta, S., et al. 2013, *A&A*, 553, A132
- Małek, K., Buat, V., Roehly, Y., et al. 2018, *A&A*, 620, A50
- Mannucci, F., Cresci, G., Maiolino, R., Marconi, A., & Gnerucci, A. 2010, *MNRAS*, 408, 2115
- McCracken, H. J., Milvang-Jensen, B., Dunlop, J., et al. 2012, *A&A*, 544, A156
- McKinnon, R., Torrey, P., Vogelsberger, M., Hayward, C. C., & Marinacci, F. 2017, *MNRAS*, 468, 1505
- Millard, J. S., Eales, S. A., Smith, M. W. L., et al. 2020, *MNRAS*, 494, 293
- Moustakas, J., Coil, A. L., Aird, J., et al. 2013, *ApJ*, 767, 50
- Mullaney, J. R., Alexander, D. M., Goulding, A. D., & Hickox, R. C. 2011, *MNRAS*, 414, 1082
- Muzzin, A., Marchesini, D., Stefanon, M., et al. 2013, *ApJ*, 777, 18
- Narayanan, D., & Davé, R. 2012, *MNRAS*, 423, 3601
- Narayanan, D., Krumholz, M., Ostriker, E. C., & Hernquist, L. 2011, *MNRAS*, 418, 664
- Narayanan, D., Krumholz, M. R., Ostriker, E. C., & Hernquist, L. 2012, *MNRAS*, 421, 3127
- Narayanan, D., Turk, M., Feldmann, R., et al. 2015, *Natur*, 525, 496
- Noeske, K. G., Weiner, B. J., Faber, S. M., et al. 2007, *ApJL*, 660, L43
- Noll, S., Burgarella, D., Giovannoli, E., et al. 2009, *A&A*, 507, 1793
- Oliver, S., Frost, M., Farrah, D., et al. 2010, *MNRAS*, 405, 2279
- Oliver, S. J., Bock, J., Altieri, B., et al. 2012, *MNRAS*, 424, 1614
- Owen, F. N. 2018, *ApJS*, 235, 34
- Pannella, M., Carilli, C. L., Daddi, E., et al. 2009, *ApJL*, 698, L116
- Pannella, M., Elbaz, D., Daddi, E., et al. 2015, *ApJ*, 807, 141
- Pantoni, L., Lapi, A., Massardi, M., Goswami, S., & Danese, L. 2019, *ApJ*, 880, 129
- Pearson, W. J., Wang, L., Hurley, P. D., et al. 2018, *A&A*, 615, A146
- Penner, K., Pope, A., Chapin, E. L., et al. 2011, *MNRAS*, 410, 2749
- Pettini, M., & Pagel, B. E. J. 2004, *MNRAS*, 348, L59
- Pillepich, A., Nelson, D., Springel, V., et al. 2019, *MNRAS*, 490, 3196
- Popping, G., Pillepich, A., Calistro Rivera, G., et al. 2021, arXiv:2101.12218
- Popping, G., Somerville, R. S., & Galametz, M. 2017, *MNRAS*, 471, 3152
- Popping, G., Somerville, R. S., & Trager, S. C. 2014, *MNRAS*, 442, 2398
- Pozzi, F., Calura, F., Zamorani, G., et al. 2020, *MNRAS*, 491, 5073
- Press, W. H., Flannery, B. P., & Teukolsky, S. A. 1986, Numerical Recipes. The Art of Scientific Computing (Cambridge: Cambridge Univ. Press)
- Puglisi, A., Daddi, E., Liu, D., et al. 2019, *ApJL*, 877, L23
- Reddy, N., Dickinson, M., Elbaz, D., et al. 2012, *ApJ*, 744, 154
- Reiter, M., Guzmán, A. E., Haworth, T. J., et al. 2020, *MNRAS*, 496, 394
- Rémy-Ruyer, A., Madden, S. C., Galliano, F., et al. 2014, *A&A*, 563, A31
- Rodighiero, G., Daddi, E., Baronchelli, I., et al. 2011, *ApJL*, 739, L40
- Rodighiero, G., Renzini, A., Daddi, E., et al. 2014, *MNRAS*, 443, 19
- Saintonge, A., Catinella, B., Tacconi, L. J., et al. 2017, *ApJS*, 233, 22
- Salim, S., Rich, R. M., Charlot, S., et al. 2007, *ApJS*, 173, 267
- Salmi, F., Daddi, E., Elbaz, D., et al. 2012, *ApJL*, 754, L14
- Salpeter, E. E. 1955, *ApJ*, 121, 161
- Santini, P., Fontana, A., Castellano, M., et al. 2017, *ApJ*, 847, 76
- Santini, P., Fontana, A., Grazian, A., et al. 2009, *A&A*, 504, 751
- Santini, P., Maiolino, R., Magnelli, B., et al. 2014, *A&A*, 562, A30
- Sargent, M. T., Daddi, E., Béthermin, M., et al. 2014, *ApJ*, 793, 19
- Schechter, P. 1976, *ApJ*, 203, 297
- Schmidt, M. 1968, *ApJ*, 151, 393
- Schreiber, C., Elbaz, D., Pannella, M., et al. 2018, *A&A*, 609, A30
- Schreiber, C., Pannella, M., Elbaz, D., et al. 2015, *A&A*, 575, A74
- Scoville, N., Aussel, H., Brusa, M., et al. 2007, *ApJS*, 172, 1
- Scoville, N., Lee, N., Vanden Bout, P., et al. 2017, *ApJ*, 837, 150
- Scoville, N., Sheth, K., Aussel, H., et al. 2016, *ApJ*, 820, 83
- Shim, H., Chary, R.-R., Dickinson, M., et al. 2011, *ApJ*, 738, 69
- Shivaei, I., Reddy, N. A., Steidel, C. C., & Shapley, A. E. 2015, *ApJ*, 804, 149
- Silverman, J. D., Daddi, E., Rodighiero, G., et al. 2015, *ApJL*, 812, L23
- Silverman, J. D., Rujopakarn, W., Daddi, E., et al. 2018, *ApJ*, 867, 92
- Simpson, J. M., Smail, I., Swinbank, A. M., et al. 2015, *ApJ*, 799, 81
- Skelton, R. E., Whitaker, K. E., Momcheva, I. G., et al. 2014, *ApJS*, 214, 24
- Sobral, D., Best, P. N., Smail, I., et al. 2014, *MNRAS*, 437, 3516
- Speagle, J. S., Steinhart, C. L., Capak, P. L., & Silverman, J. D. 2014, *ApJS*, 214, 15
- Steinhart, C. L., Speagle, J. S., Capak, P., et al. 2014, *ApJL*, 791, L25
- Symeonidis, M., Vaccari, M., Berta, S., et al. 2013, *MNRAS*, 431, 2317
- Tacchella, S., Dekel, A., Carollo, C. M., et al. 2016, *MNRAS*, 457, 2790
- Tacconi, L. J., Genzel, R., Neri, R., et al. 2010, *Natur*, 463, 781
- Tacconi, L. J., Genzel, R., Saintonge, A., et al. 2018, *ApJ*, 853, 179
- Tacconi, L. J., Genzel, R., & Sternberg, A. 2020, *ARA&A*, 58, 157
- Tacconi, L. J., Neri, R., Genzel, R., et al. 2013, *ApJ*, 768, 74
- Tadaki, K.-i., Genzel, R., Kodama, T., et al. 2017, *ApJ*, 834, 135
- Tan, Q., Daddi, E., Magdis, G., et al. 2014, *A&A*, 569, A98
- Tasca, L. A. M., Le Fèvre, O., Hathi, N. P., et al. 2015, *A&A*, 581, A54
- Tristram, K. R. W., Meisenheimer, K., Jaffe, W., et al. 2007, *A&A*, 474, 837
- Urry, C. M., & Padovani, P. 1995, *PASP*, 107, 803
- Valentino, F., Magdis, G. E., Daddi, E., et al. 2020, *ApJ*, 890, 24
- van der Wel, A., Chang, Y.-Y., Bell, E. F., et al. 2014, *ApJL*, 792, L6
- Vijayan, A. P., Clay, S. J., Thomas, P. A., et al. 2019, *MNRAS*, 489, 4072
- Walter, F., Decarli, R., Aravena, M., et al. 2016, *ApJ*, 833, 67
- Wang, T., Elbaz, D., Schreiber, C., et al. 2016, *ApJ*, 816, 84
- Weigel, A. K., Schawinski, K., & Bruderer, C. 2016, *MNRAS*, 459, 2150
- Whitaker, K. E., Franx, M., Bezanson, R., et al. 2015, *ApJL*, 811, L12
- Whitaker, K. E., Franx, M., Leja, J., et al. 2014, *ApJ*, 795, 104
- Whitaker, K. E., van Dokkum, P. G., Brammer, G., & Franx, M. 2012, *ApJL*, 754, L29
- Williams, C. C., Spilker, J. S., Whitaker, K. E., et al. 2021, *ApJ*, 908, 54
- Zahid, H. J., Bresolin, F., Kewley, L. J., Coil, A. L., & Davé, R. 2012, *ApJ*, 750, 120